HAL
open science

The Faraday rotation effect in Saturn Kilometric Radiation observed by the CASSINI spacecraft

Ulrich Taubenschuss, Laurent Lamy, Georg Fischer, David Píša, Ondřej Santolík, Jan Souček, William S Kurth, Baptiste Cecconi, Philippe Zarka, Helmut O Rucker

To cite this version:

Ulrich Taubenschuss, Laurent Lamy, Georg Fischer, David Píša, Ondřej Santolík, et al.. The Faraday rotation effect in Saturn Kilometric Radiation observed by the CASSINI spacecraft. Icarus, 2021, 370, pp.114661. 10.1016/j.icarus.2021.114661 . hal-03367845

HAL Id: hal-03367845

https://hal.science/hal-03367845v1

Submitted on 6 Oct 2021

HAL is a multi-disciplinary open access archive for the deposit and dissemination of scientific research documents, whether they are published or not. The documents may come from teaching and research institutions in France or abroad, or from public or private research centers.

L'archive ouverte pluridisciplinaire **HAL**, est destinée au dépôt et à la diffusion de documents scientifiques de niveau recherche, publiés ou non, émanant des établissements d'enseignement et de recherche français ou étrangers, des laboratoires publics ou privés.

Icarus 370 (2021) 114661

Contents lists available at ScienceDirect

Icarus

journal homepage: www.elsevier.com/locate/icarus

Research Paper

The Faraday rotation effect in Saturn Kilometric Radiation observed by the CASSINI spacecraft

Ulrich Taubenschuss [a,*], Laurent Lamy [c,d], Georg Fischer [e], David Píša [a], Ondřej Santolík [a,b], Jan Souček [a], William S. Kurth [g], Baptiste Cecconi [c], Philippe Zarka [c], Helmut O. Rucker [f]

[a] Department of Space Physics, Institute of Atmospheric Physics of the Czech Academy of Sciences, Prague, Czechia
[b] Faculty of Mathematics and Physics, Charles University, Prague, Czechia
[c] LESIA, Observatoire de Paris, Université PSL, CNRS, Sorbonne Université, Université de Paris, Meudon, France
[d] Aix Marseille Université, CNRS, CNES, LAM, Marseille, France
[e] Space Research Institute, Austrian Academy of Sciences, Graz, Austria
[f] Commission for Astronomy, Austrian Academy of Sciences, Graz, Austria
[g] Department of Physics and Astronomy, The University of Iowa, Iowa City, USA

ARTICLE INFO

Keywords:
Cassini
Saturn kilometric radiation
Faraday rotation

ABSTRACT

Non-thermal radio emissions from Saturn, known as Saturn Kilometric Radiation (SKR), are analyzed for the Faraday rotation effect detected in Cassini RPWS High Frequency Receiver (HFR) observations. This phenomenon, which mainly affects the lower-frequency part of SKR below 200 kHz, is characterized by a rotation of the semi-major axis of the SKR polarization ellipse as a function of frequency during wave propagation through a birefringent plasma medium. Faraday rotation is found in 4.1% of all HFR data recorded by Cassini above 20 degrees northern and southern magnetic latitude, from mid-2004 to late 2017. A statistical visibility analysis shows that elliptically polarized SKR from the dawn source regions, when beamed toward high latitudes into the noon and afternoon local time sectors, is most likely to experience Faraday rotation along the ray path. The necessary conditions for Faraday rotation are discussed in terms of birefringent media and sharp plasma density gradients, where SKR (mostly R-X mode) gets split into the two circularly polarized modes R-X and L-O. By means of a case study we also demonstrate how Faraday rotation provides an estimate for the average plasma density along the ray path.

1. Introduction

Saturn kilometric radiation (SKR) is a strong non-thermal radio emission that is generated by unstable electron populations inside the magnetosphere of Saturn (Kaiser et al., 1980; Warwick et al., 1981; Lamy, 2017). Radio sources are distributed along auroral magnetic field lines at radial distances of $1.1\,R_S < r < 6\,R_S$ ($1\,R_S = 60\,268$ km). There is a direct connection between the intensity of SKR and the brightness of Saturn's auroral oval in ultraviolet and infrared light (Kurth et al., 2005; Lamy et al., 2009, 2013). Amplified SKR frequencies are at or slightly below the local electron cyclotron frequency, f_c, inside the source region, spanning over a total frequency range of ~1 kHz to ~1.2 MHz. In general, a mechanism known as the "cyclotron maser instability" (CMI) is responsible for amplification of radio waves at the expense of electron kinetic energy under conditions of electron cyclotron resonance (Wu and Lee, 1979). The resonance condition is fulfilled by mildly relativistic electrons at energies of a few keV that are part of a ring-type or shell distribution in velocity space (Mutel et al., 2010). Positive wave growth rates are achieved inside low density plasma regions where the ratio of electron plasma frequency, f_p, to cyclotron frequency corresponds to $f_p/f_c < 0.1$ (Lamy et al., 2010; Kurth et al., 2011; Menietti et al., 2011; Lamy et al., 2018). The same mechanism also acts at the other radio planets of our solar system, i.e., at Earth, Jupiter, Uranus and Neptune (Zarka, 1998).

Once generated, SKR is propagating either in the R-X mode or the L-O mode (Lamy et al., 2008). The initial polarization at the source is nearly linear (Lamy et al., 2011), but gets gradually shifted from linear toward circular at greater distances. When beamed toward higher latitudes, it was found that elliptically polarized parts remain present among emission that has become already almost 100% circular (Fischer et al., 2009). This phenomenon is known as "limiting polarization" (Budden, 1952; Hayes, 1971) that occurs when an electromagnetic wave enters a region of very low plasma density (free space). Coupling among the possible modes of propagation prevents the wave from

* Corresponding author.
E-mail address: ut@ufa.cas.cz (U. Taubenschuss).

https://doi.org/10.1016/j.icarus.2021.114661
Received 5 March 2021; Received in revised form 12 July 2021; Accepted 11 August 2021
Available online 28 August 2021
0019-1035/© 2021 The Author(s). Published by Elsevier Inc. This is an open access article under the CC BY-NC-ND license (http://creativecommons.org/licenses/by-nc-nd/4.0/).

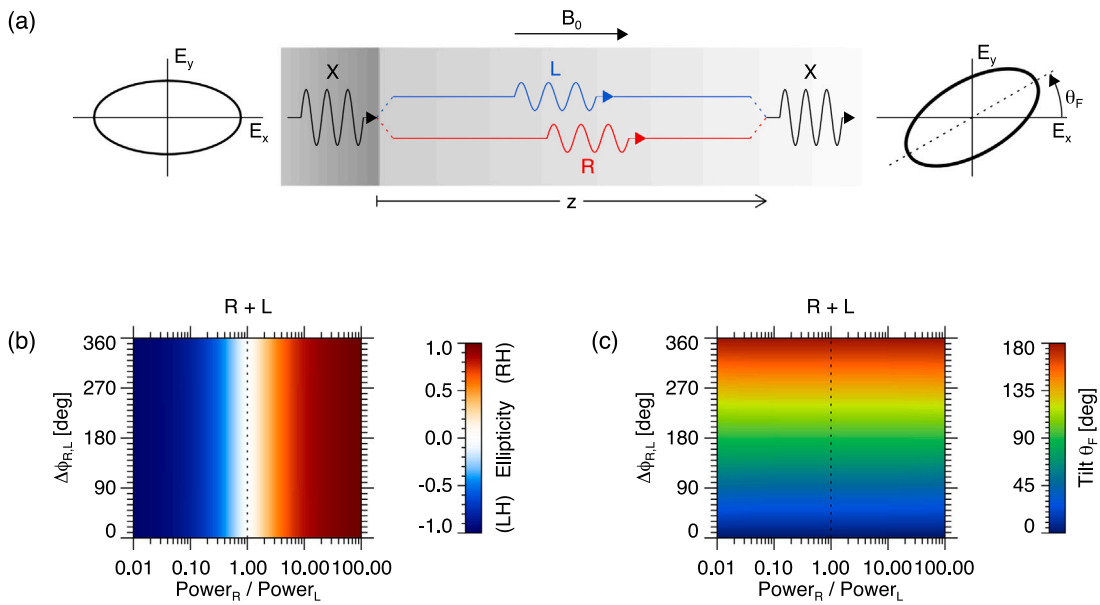

Fig. 1. (a) Illustration of an elliptically polarized plane wave (X-mode) propagating through a birefringent medium. Gray shades shall indicate plasma density. The sharp transition from dark to light shades marks a discontinuity in the plasma, where the ray splits into an R-mode and an L-mode. Results for a superposition of R-mode and L-mode in terms of (b) ellipticity and (c) rotation angle θ_F are plotted as a function of relative wave power (x-axis) and phase shift (y-axis).

adapting its polarization to the local plasma conditions. In case of an X-mode as a primary wave, part of the wave's energy converts into an O-mode, and the coupling between both modes keeps the polarization constant, i.e., elliptical. Before the zone of limiting polarization is reached, the linear part of elliptically polarized SKR can be susceptible to the Faraday rotation effect, which becomes apparent as a rotation of the axis of linear polarization as a function of frequency. Most evidence for a natural occurrence of Faraday rotation comes from ground-based observations on Earth's surface, where radio waves from extraterrestrial sources first need to pass through Earth's ionosphere and plasmasphere, thereby experiencing strong Faraday rotation along the ray path (Warwick and Dulk, 1964; Goertz, 1974; Lecacheux et al., 1991; Ladreiter et al., 1995; Oberoi and Lonsdale, 2012).

In case of an elliptically polarized wave, Faraday rotation manifests itself as a change of the orientation of the semi-major axis of the polarization ellipse. This scenario is sketched in Fig. 1a. As elliptically polarized SKR encounters a discontinuity in the plasma, e.g., a sharp density gradient, it splits into two circularly polarized modes of opposite sense: a right-hand circularly polarized R-mode, and a left-hand circularly polarized L-mode. The splitting of one incident mode into two modes can again be described by the theory of mode coupling, but is now of a different kind than the one responsible for the limiting polarization mentioned above (see e.g., Cheng and Fung, 1977, Fung and Cheng, 1977, or Budden, 1985). After passing through the density gradient, the two modes continue to propagate through a medium which is slowly varying with distance, where mode coupling is negligible, and which is said to be "birefringent", i.e., it provides significantly different refractive indices for different wave modes. Furthermore, for Faraday rotation to occur, the ambient magnetic field, $\mathbf{B_0}$, needs to be oriented parallel or quasi-parallel to the wave vectors so that both modes remain circularly polarized during propagation. In Fig. 1a, the R-mode and L-mode are sketched to superpose again at some distance z to the entry point. By superposition we mean a sum of electric and magnetic fields. The location of superposition can either be the point where the medium loses its birefringent properties, e.g., the rays enter the zone of limiting polarization and free space afterwards, or it can be the point of measurement at the antenna system of Cassini. Along the distance z, the R-mode and L-mode accumulate a phase shift relative to each other due to different phase velocities in the birefringent medium. Upon superposition, the phase shift manifests itself as a rotation of the linear axis of polarization of the resulting wave relative to its initial orientation. This is illustrated on the right-hand side of Fig. 1a. In case of elliptically polarized SKR, the rotation is applied to the semi-major axis of the polarization ellipse. The Faraday rotation angle is indicated by θ_F.

The classical scenario deals with R-mode and L-mode waves of equal power. Their product of superposition is linearly polarized (see also dotted line in Fig. 1b), and the Faraday rotation angle θ_F can be analytically derived as (Bittencourt, 2004)

$$\theta_F = \frac{\Delta\phi_{R,L}}{2} = \frac{z\,(k_L - k_R)}{2} \,. \tag{1}$$

The phase shift $\Delta\phi_{R,L}$ depends on the propagation distance z and on the wave numbers k_L and k_R of the L-mode and the R-mode, respectively. The wave numbers are defined through the dispersion relation. Inserting wave numbers for a cold plasma and using a quasi-parallel approximation ($\mathbf{k} \sim\parallel \mathbf{B_0}$, $f \gg f_c$, $f \gg f_p$) (Gurnett and Bhattacharjee, 2017; Thompson et al., 2017), one gets

$$\theta_F = \frac{e^3}{8\pi^2\,\varepsilon_0\,m_e^2\,c\,f^2} \int_0^z n_e(z)\,B_0(z)\,\cos\theta_k\,dz \,. \tag{2}$$

As can be seen, θ_F depends on the integrated electron density n_e, the magnetic field strength B_0 and the cosine of the wave normal angle θ_k along the ray path. Furthermore, θ_F has a dependence on $1/f^2$, where f is the wave frequency. All other quantities in Eq. (2) are constants: e and m_e are charge and rest mass of an electron, respectively, and c and ε_0 are the speed of light and the permittivity in vacuum, respectively.

The quasi-parallel approximation from Eq. (2) is based on the assumption of small θ_k and a wave frequency that is significantly larger than f_p and f_c. An $f_{SKR} \gg f_p$ is definitely fulfilled close to the SKR source region and throughout the high-latitude magnetosphere of Saturn. An $f_{SKR} \gg f_c$ is only justified at a sufficient distance to the source. However, as will be discussed later, the purpose of this study is not to derive a precise absolute rotation angle for a single frequency, but to interpret relative rotation angles across a broader range of frequencies. For that purpose, the quasi-parallel approximation from Eq. (2) is sufficient.

A dependence of θ_F on frequency will generate a regular modulation of intensity as a function of frequency in a linearly polarized antenna (monopole or dipole, stably mounted), or in the cross-spectral power

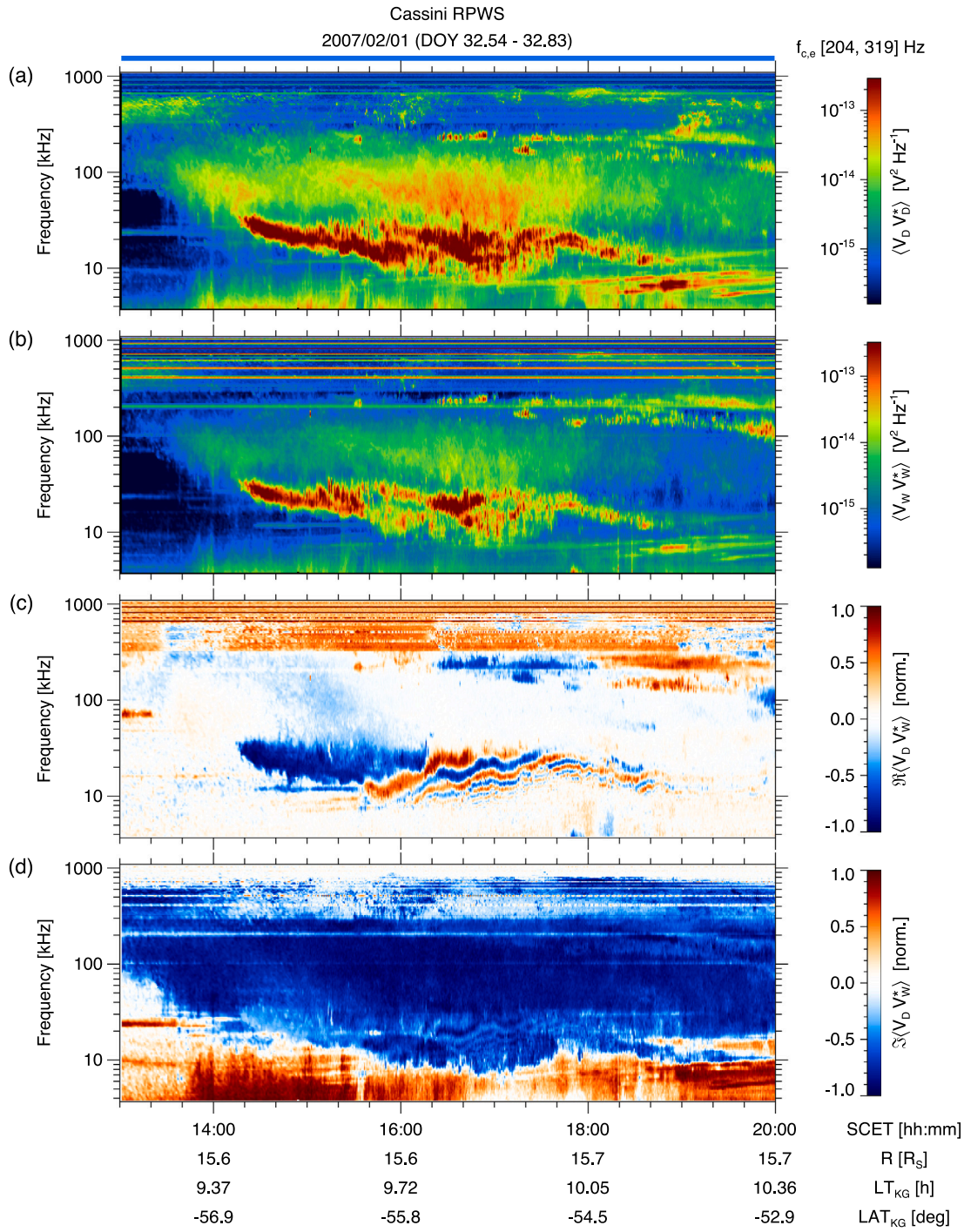

Fig. 2. A summary of Cassini RPWS/HFR observations in 2-antenna mode from February 1, 2007. (a) Auto-power spectral density in the dipole antenna, (b) auto-power spectral density in the w-antenna, (c) real part (including Faraday fringes) and (d) imaginary part of the cross-power spectral density between both antennas. Time and spacecraft coordinates (kronographic) are given at the bottom. (For interpretation of the references to color in this figure legend, the reader is referred to the web version of this article.)

between two linear antennas. These spectral modulations are often referred to as "Faraday fringes". An example is presented in Fig. 2. In principle, a measurement of θ_F, together with the knowledge of the ray's exact path between the entry point and the exit point from the birefringent medium, allows one to infer the original orientation angle, θ_{F0}, of the polarization ellipse at the entry point. Matters simplify further if we can assume that all frequency components of a broadband emission took an identical path through the medium and that they started with approximately identical orientation angles. Then, an extrapolation of the measured $[f, \theta_F]$-curve to $f \to \infty$ directly yields an estimate for θ_{F0} (Boudjada and Lecacheux, 1991). However, significant fluctuations in the retrieved θ_F-values due to a violation of the assumptions mentioned above often do prevent a reliable determination of θ_{F0} (Ladreiter et al., 1995).

For a proper description of Faraday rotation in elliptically polarized SKR, one might assume that the classical scenario cannot be applied because of its limitation to linearly polarized waves. However, it can be shown that a superposition of R-mode and L-mode waves will result in an elliptically polarized wave if both modes are not of equal but of different power. Figs. 1b,c present results from a numerical simulation

of a superposition of R-mode and L-mode, which are both modeled as circularly polarized plane waves. The shape and orientation of the polarization ellipse as a result of superposition are analyzed in terms of the relative wave power and the relative phase shift between R-mode and L-mode. As can be seen from the ellipticity in Fig. 1b, the stronger mode defines the sense of polarization of the superposition product. The ellipticity corresponds to the ratio of semi-minor to semi-major axis of the polarization ellipse, and its sign specifies right-handed (> 0) or left-handed (< 0). Equal powers of R-mode and L-mode will result in a linearly polarized wave (ellipticity = 0; white color). In order to get RH-polarized X-mode SKR, the R-mode needs to be stronger than the L-mode upon superposition. Fig. 1c demonstrates that the rotation angle θ_F is only a function of phase shift, but not of relative power. Thus, Eqs. (1) and (2) can be directly applied to the elliptically polarized scenario as well.

First detections of Faraday rotation in SKR have been noted by Lecacheux (2011). The present work constitutes the first comprehensive analysis in this context. In Section 2, the Cassini instruments and relevant data products are briefly discussed. Section 3 presents results from a statistical analysis of all Faraday rotation events which have been detected during Cassini's orbital phase of the mission. A model for the necessary source–observer geometry is discussed in Section 4, which is then compared to results from a goniopolarimetric study in Section 5. This section also demonstrates a technique for deriving an estimate of the plasma density along the SKR ray path. Section 6 finishes with the conclusions.

2. Dataset and methodology

The Cassini spacecraft is equipped with three 10 m long electric monopole antennas named u, v and w. The tri-axial antenna system, together with a set of different receivers, forms the Radio and Plasma Wave Science (RPWS) investigation (Gurnett et al., 2004) for analyzing SKR across its entire frequency range. We will focus our analysis on data obtained by the High Frequency Receiver (HFR) system (Cecconi et al., 2017a). The RPWS instrument can either be operated in a 2-antenna mode (survey mode) or a 3-antenna mode (goniopolarimetric mode). In the 2-antenna mode, the voltages V_u and V_v, which are measured along the u and the v antenna, respectively, are combined to a virtual dipole $V_D = V_u - V_v$ which provides better sensitivity and improved noise characteristics. The signal V_w from the w-antenna is always available.

Assuming SKR to propagate as a plane wave that is measured at a sufficient distance from the source region, the wave's polarization state can be expressed in terms of the two-dimensional Stokes parameters S, Q, U and V (Cecconi and Zarka, 2005; Taubenschuss and Santolík, 2019). Note that Stokes-V should not be confused with voltage from an antenna. These four Stokes parameters can be defined in the wave-frame, which has a z-axis that points along the direction of the wave vector $\mathbf{k}$. The polarization ellipse lies inside the $[x, y]$-plane of the wave-frame, with the semi-major axis rotated with respect to the x-axis about the angle τ. This angle also includes a possible Faraday rotation angle θ_F. τ is computed from the two Stokes parameters U and Q as

$$\tau = 0.5 \arctan(U/Q) \ . \tag{3}$$

Q is measured as a difference of electric auto-power spectral density along the x-axis and the y-axis, i.e.,

$$Q = \langle E_x E_x^* \rangle - \langle E_y E_y^* \rangle \ . \tag{4}$$

The complex electric amplitudes E_x and E_y are connected to the measured voltages via the antenna effective length vectors (Vogl et al., 2004). The parentheses $\langle \ldots \rangle$ in Eq. (4) indicate spectral averaging, and a *-symbol denotes the complex conjugate. The Stokes parameter U is proportional to the real part of the cross-spectral power between E_x and E_y:

$$U = 2\,\Re\langle E_x E_y^* \rangle \ . \tag{5}$$

For getting a first evidence for the presence of Faraday rotation in SKR, it is actually sufficient to just investigate the quantity $\Re\langle E_x E_y^* \rangle$. Furthermore, it is sufficient to use directly measured voltages and their cross-spectral products, without a transformation into electric amplitudes inside the wave-frame. E_y is replaced with the Fourier-transformed V_w from the w-antenna. E_x can either be the voltage from the u-antenna, the v-antenna, or the dipole antenna. Systematic variations in $\Re\langle V_u V_w^* \rangle$, $\Re\langle V_v V_w^* \rangle$ and $\Re\langle V_D V_w^* \rangle$ as a function of frequency should clearly indicate the presence of the Faraday rotation effect.

An example for Faraday rotation in SKR is presented in Fig. 2. It shows, from top to bottom, auto-power spectral density in (a) the dipole antenna $\langle V_D V_D^* \rangle$ and (b) the w-antenna $\langle V_w V_w^* \rangle$, as well as (c) the real part $\Re\langle V_D V_w^* \rangle$ and (d) the imaginary part $\Im\langle V_D V_w^* \rangle$ of the cross-spectral power between both antennas. SKR is visible as intense emission above ~7 kHz and up to ~900 kHz. A closer inspection of Fig. 2c reveals that $\Re\langle V_D V_w^* \rangle$ undergoes systematic oscillations as a function of frequency between 7 and 30 kHz. Changes from positive (red) to negative (blue) values and vice versa indicate changes in the orientation angle τ of the polarization ellipse. It should be noted that $\Re\langle V_D V_w^* \rangle$ is multiplied with the normalization factor $1/\sqrt{\langle V_D V_D^* \rangle \langle V_w V_w^* \rangle}$ in order to transform values into the range -1 to $+1$.

The systematic variations seen here in $\Re\langle V_D V_w^* \rangle$ are the Faraday fringes. They should also manifest themselves as variations in intensity in Fig. 2a and Fig. 2b, causing variations in the Stokes parameter Q from Eq. (4). However, this is barely visible in Fig. 2a,b because natural intensity fluctuations of SKR seen in one antenna stretch over a much larger dynamic range.

Above 30 kHz, $\Re\langle V_D V_w^* \rangle$ is mostly close to zero (white color), except a few banded SKR structures seen after 16:00 SCET above 100 kHz. Some of these bands, as well as the low-frequency part of SKR at $f < 30$ kHz including the Faraday fringes, are elliptically polarized. The rest belongs to circularly polarized SKR. In fact, the degree of circular polarization can be estimated from Fig. 2d since it is proportional to $\Im\langle V_D V_w^* \rangle$. Due to the momentary orientation of Cassini (magnetometer boom pointing away from Saturn) and its position at southern kronographic (KG) latitudes of $-57°$ to $-53°$, X-mode SKR emitted from the southern auroral region is seen with an $\Im\langle V_D V_w^* \rangle < 0$ (blue shades). The banded emissions below 10 kHz with $\Im\langle V_D V_w^* \rangle > 0$ (red shades) are "narrowband" emissions, which are propagating in the O-mode at frequencies above the local electron cyclotron and plasma frequency (Ye et al., 2009).

3. Statistical visibility analysis

The Faraday rotation effect in SKR is sporadically visible during 159 out of 293 orbits of Cassini around Saturn during the years 2004–2017. A total number of 611 individual events are identified, which fulfill the property of continuous visibility of Faraday fringes in SKR dynamic spectra. Fringe patterns are especially clearly visible in the normalized real part of the cross-spectral power between two antennas because this quantity is directly proportional to the Stokes parameter U and furthermore to τ (see also Eqs. (3) and (5)). Hereafter, these "Faraday rotation events" will be abbreviated as **FRE**s. They have been identified manually by browsing through all available Cassini RPWS/HFR data. The final number of 611 events is the result of already excluding unclear or questionable cases from a larger pool of 1050 events. We demand a clear visibility of fringe patterns for more than 10 min and a minimum of two full fringe modulation periods along the frequency axis.

3.1. Time and frequency

Statistical results on the time and frequency behavior of FREs are presented in Fig. 3. The entire spectral region covered by SKR emission is indicated by a gray shaded area in Fig. 3a, and parts affected by Faraday rotation are highlighted by colored horizontal lines (the fringes).

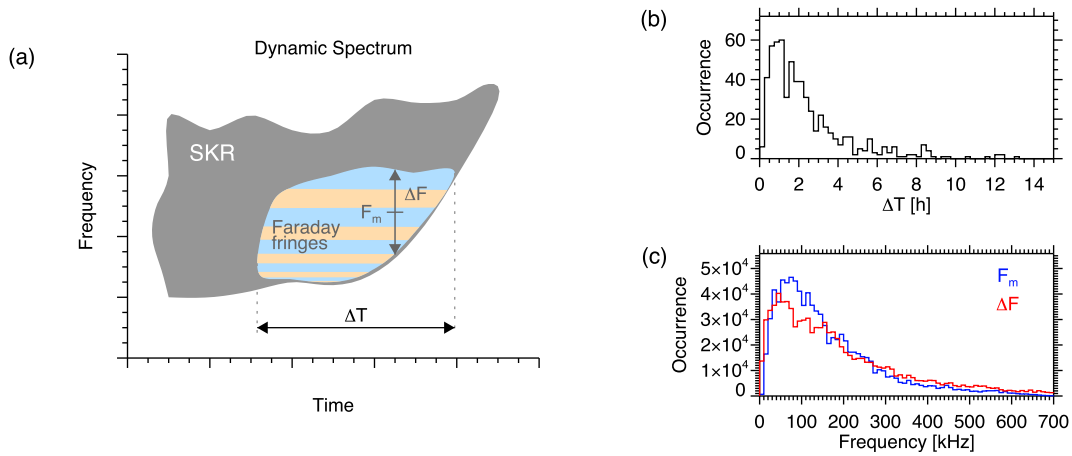

Fig. 3. (a) Sketch of an FRE (Faraday Rotation Event) observed in an SKR dynamic spectrum, (b) occurrence distribution of time duration ΔT for all events, and (c) occurrence distribution of instantaneous frequency bandwidth ΔF (red) and instantaneous middle frequency F_m (blue) for all events. (For interpretation of the references to color in this figure legend, the reader is referred to the web version of this article.)

For each event, its duration ΔT, its instantaneous frequency bandwidth ΔF and its instantaneous middle frequency F_m are recorded. These three parameters characterize the spectral area covered by Faraday fringes. One event yields one value for ΔT but many values for ΔF and F_m at each instant in time. In order to account for different temporal resolutions used for HFR recordings throughout the Cassini mission, scanned values across all events are interpolated to a common time axis with 6 s resolution, which is lower than the best possible resolution of 8 s found in our dataset. This ensures that derived count rates are independent of the instrumental mode of observation.

Fig. 3b shows the occurrence distribution of ΔT. FREs typically last one hour, with their number exponentially decreasing toward longer observation intervals. Rare events have been found with a continuous visibility of Faraday fringes for up to 13 h, i.e., for more than one full planetary rotation (~10.7 h). Summing over ΔT from all 611 events yields a total time of ~1500 h. A normalization to the total time Cassini spent in orbit around Saturn results in an average occurrence rate of merely 1.3%. This number can be increased up to 4.1% when considering only high latitude passes, i.e., when Cassini is above ~20° northern and southern latitude. The latitudinal dependence of occurrence will be discussed in more detail in Section 3.2. For now, we can conclude that FREs are a truly rare phenomenon.

Fig. 3c is a histogram of occurrences for the frequency-related parameters F_m and ΔF. Note that the numbers shown along the y-axis in Fig. 3c do not correspond to the number of events anymore, as is the case in Fig. 3b, but they correspond to the number of 6 s-instances in time. As can be seen, Faraday fringes are most commonly found in the lower frequency range of SKR, with F_m-occurrences peaking around 80 kHz (see blue line in Fig. 3c). Maximum SKR frequencies that can get modulated by Faraday fringes are found up to 1 MHz, i.e., close to the upper frequency cutoff of SKR. The red line, which depicts the occurrence distribution of ΔF, has a very similar profile to that of F_m. It indicates that ΔF tends to be proportional to F_m, with Faraday fringes covering a larger range at higher frequencies, and becoming more narrow at lower frequencies. Of course, $F_m + \Delta F/2$ never exceeds the upper frequency cutoff of SKR at about 1.2 MHz.

3.2. Orbital position of Cassini

The occurrence rate of FREs from the perspective of Cassini is investigated in terms of the following trajectory parameters: radial distance, latitude, local time and SLS5 longitude of Cassini. We choose coordinates from the non-spinning kronographic (KG) system ($[x, z]$-plane contains the direction toward the sun) because this system has a z-axis that is closely aligned with Saturn's magnetic dipole axis. Results are summarized in Fig. 4.

The central panel of Fig. 4a is a 2-dimensional histogram showing the occurrence of FREs in dependence of Cassini's local time (x-axis) and latitude (y-axis). The color in each bin represents an occurrence which is computed from the amount of time Cassini observes FREs, and normalized by the total amount of time Cassini spent in the bin. It is fairly obvious from Fig. 4a that FREs are visible only for an observer located above ~20° latitude. A 1D-histogram for occurrence with latitude is plotted on the right-hand side of Fig. 4a (aligned vertically). Absolute count rates of FREs in the northern hemisphere are higher than in the southern hemisphere, but since Cassini spent more time in the northern hemisphere during its mission, a normalization yields a higher occurrence in the southern hemisphere (see red vertical histogram). Absolute count rates with regard to latitude are illustrated in Fig. 4c. Counts are converted to the amount of time for which FREs are visible in each bin. Fig. 4c is an accumulation of meridional planes across all local times. As can be seen, FREs are most frequent in SKR that is beamed toward ~45° latitude in both hemispheres. Furthermore, most FREs are observed inside 20 R_S radial distance, with detections as close as $r \sim 1.6\,R_S$, but also as far out as $r \sim 70\,R_S$. With regard to latitude, an upper limit of ~72° is explained by the fact that Cassini's orbits did not reach beyond that point. A lower limit of LAT ~ 20° is most probably due to SKR becoming almost 100% circularly polarized below that latitudinal threshold. Faraday rotation becomes invisible inside radiation that has no degree of linear polarization. The latitudinal threshold from this study is roughly in line with Fischer et al. (2009) who found elliptical SKR polarization mainly above 30° in latitude from a more limited data set of Cassini's first episode of high-latitude excursions.

Besides a strong dependence on latitude, FRE occurrence also exhibits a structuring with local time. From the bottom and top panels in Fig. 4a we see that occurrences are clearly higher in the noon/afternoon sector in both hemispheres. This is also evident in Fig. 4d and Fig. 4e when looking at the absolute count rates (visibility times). It should be noted that the gap in FRE occurrence seen around 13:00–14:00 LT in the southern hemisphere is indeed an artifact of Cassini's orbit geometry, meaning that Cassini spent almost no time at high southern latitudes within this limited LT-sector. For all other LT-sectors we have plenty of observation time available, and any remaining asymmetry in the data, especially after normalization of absolute count rates, should reflect the intrinsic occurrence of FREs. FREs are indeed more frequently observed on the dayside, with a strong preference toward the noon/afternoon sector. This peculiarity will be further discussed in Section 4 in connection with the special SKR beaming geometry and the ability of SKR to illuminate Saturn's high-latitude magnetosphere.

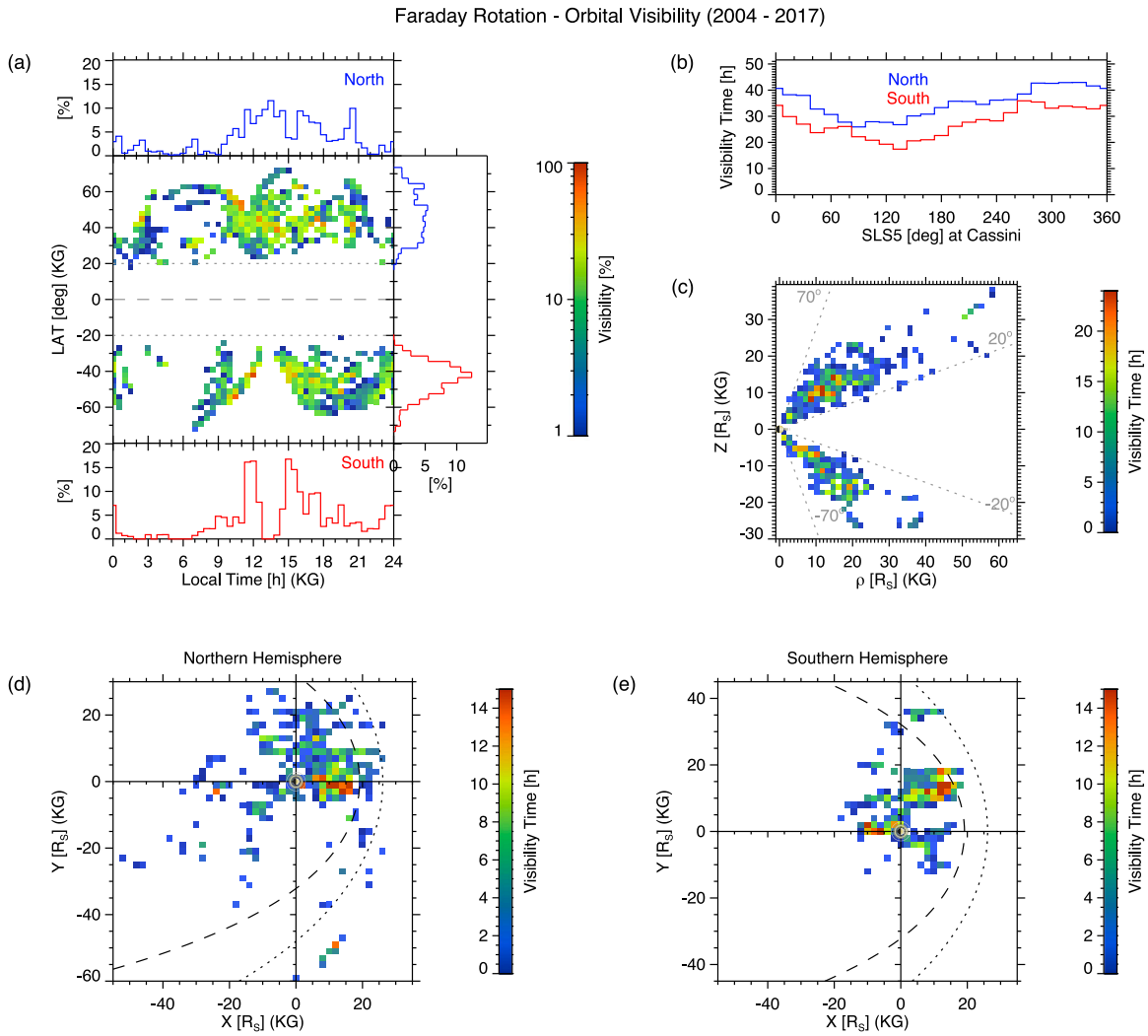

Fig. 4. Distribution of FREs in the non-spinning kronographic (KG) coordinate system, as a function of (a) local time and latitude, (b) SLS5 longitude, and (c) ρ ($= \sqrt{X^2 + Y^2}$) and Z inside the meridional plane. (d, e) A projection of distributions onto the equatorial plane for observations in the northern and southern hemisphere, respectively. Absolute count rates are given in hours (visibility time) and relative counts are given in percent (visibility times normalized to the total time Cassini spent in a bin). In (d,e), the magnetopause and the bow shock for average solar wind conditions are indicated by dashed and dotted lines, respectively (Kanani et al., 2010; Went et al., 2011).

Finally, we comment on a possible dependence with longitude. The newest rotating longitude system available is the SLS5 system from Ye et al. (2018). This system takes into account two different periods in the northern and southern hemispheres with which SKR power from the main source on the morning side is modulated in a clock-like fashion. Both periods are interpreted as independent rotation periods for the two hemispheres of Saturn. Since Faraday rotation is observed only when Cassini is at medium to high latitudes, it is easy to attribute observations to either the northern or southern SLS5 system by assuming that the hemisphere of the SKR source region is identical to the hemisphere of SKR observation from that very same source region. This task would be difficult from a vantage point close to the equatorial plane where SKR from both hemispheres is simultaneously visible. Fig. 4b shows that there is a shallow modulation of visibility time with SLS5 longitude at the position of the spacecraft. The phase of modulation is almost the same in both hemispheres. FRE occurrence peaks when an SLS5 $\sim 320°$ is pointing toward Cassini. This peak must be interpreted in terms of the zero-level of the SLS5 system. For each full rotation, SLS5 $= 0°$ is calibrated to the longitude at the subsolar point while SKR is reaching its peak power. So, an SLS5 $\sim 320°$ at Cassini probably means that FREs are preferentially observed while SKR passes through its phase of peak power. During that time, Cassini is not always exactly positioned at the subsolar point, otherwise a peak in FRE occurrence would be evident at SLS5 $\sim 0°$. The fact that FRE occurrence peaks at SLS5 $\sim 320°$ means that Cassini is usually positioned a little bit beyond noon, i.e., in the afternoon sector, where SLS5 $< 0°$. This correlates well with the occurrence in local time presented in Fig. 4a,d,e. So, a modulation of FRE occurrence with SLS5 longitude seems to result from a rotational modulation of SKR intensity, with FREs being more frequently observed in more powerful SKR emission.

Along with SKR intensity, rotational modulations have also been found in magnetic field and plasma observations. These are commonly referred to as "planetary period oscillations" (for a review see Carbary and Mitchell, 2013). The variation of FRE occurrence seen in Fig. 4b suggests that the essential conditions for Faraday rotation, i.e., the presence of a sharp density gradient and a birefringent medium, might be prone to rotational modulations as well. We will discuss this issue further in Section 6 in connection with theories for the origin of strong density gradients found at high latitudes (Gurnett et al., 2010; Thomsen et al., 2015a).

3.3. Long-term variations

Fig. 5a is a summary of 11 years of FRE observations in SKR, from the first detections by Cassini in September 2006 until the end of the

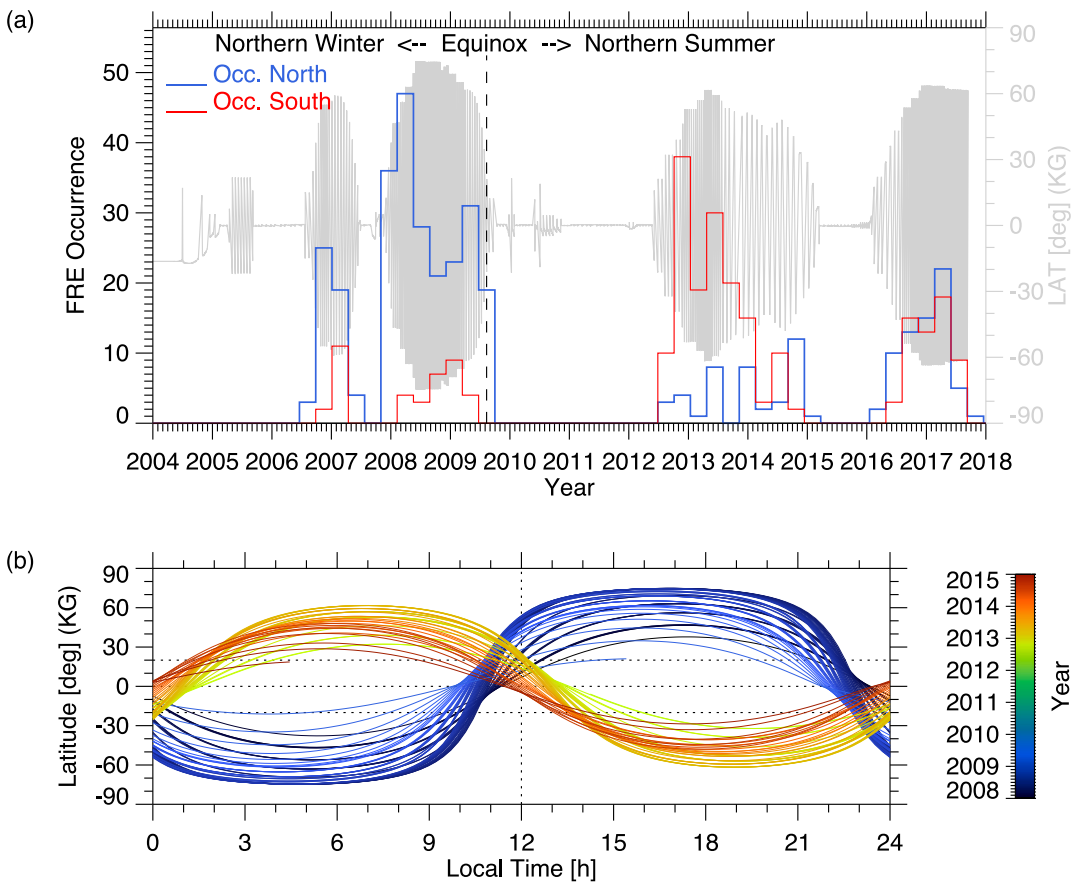

Fig. 5. (a) Histograms for FREs as a function of time for the northern (blue) and southern (red) hemisphere observations. The bin size is 100 days. Cassini's KG-latitude is plotted in gray in the background (see axis on the right-hand side). (b) KG-latitude of Cassini versus local time for two selected time periods: November 2007 until September 2009 (blue) and July 2012 until February 2015 (yellow/orange/red). (For interpretation of the references to color in this figure legend, the reader is referred to the web version of this article.)

mission in September 2017. Histograms for FRE occurrence are separated with regard to the hemisphere of observation, i.e., with regard to the hemisphere of the corresponding SKR source region. The histogram for northern hemisphere data is shown in blue color, and southern hemisphere data are in red. As already pointed out earlier, there is a clear correspondence between the visibility of FREs and Cassini's magnetic latitude. The latter is included in Fig. 5a in gray color. There are four major episodes of high-latitude excursions visible, and Faraday rotation has been observed during all of them. The histogram for the northern hemisphere indicates more FREs before equinox (August 11, 2009; dashed vertical line), i.e., during northern winter. After equinox, the situation seems to reverse, with FREs detected more frequently in the southern hemisphere. This may imply that FREs are following a seasonal trend and that the momentary winter hemisphere is producing more FREs than the spring/summer hemisphere. However, such a result is surprising because ionospheric conductivities and associated auroral currents and SKR intensities are expected to be stronger during summer conditions (Kimura et al., 2013; Bradley et al., 2018; Hunt et al., 2018; Nakamura et al., 2019). This issue will be discussed in more detail in Section 6. In the following, we want to provide evidence that a putative seasonal variation can as well be attributed to an orbital selection effect. It has been shown in Fig. 4a and d that there is a strong accumulation of FREs in the noon/afternoon local time sectors. The KG-latitude of Cassini as a function of local time is plotted in Fig. 5b. Data from two intervals of increased FRE occurrence are picked: the interval from the end of 2007 until the middle of 2009, which is before/at equinox (blue shades), and the interval from the middle of 2012 until the beginning of 2015, which is after equinox (yellow/orange/red shades). As can be seen, a higher occurrence rate of FREs in the northern hemisphere before equinox is linked to a dominant coverage of the noon/afternoon LT-sector with high northern latitudinal positions of Cassini. On the other hand, southern hemisphere observations are performed inside the dawn LT-sector, where FREs are rare. After equinox, the geometry of Cassini's orbits has been gradually changing, so that after 2012, the afternoon sector was predominantly observed from high southern latitudes. Consequently, the occurrence rate of FREs for southern hemisphere observations is increasing. The reasons for a strong orbital bias with latitude and local time will be discussed in Section 4 in terms of the special beaming geometry of SKR.

3.4. Frequency and position

We also investigate if there is a possible connection between the position of Cassini and the instantaneous range of frequencies which are affected by Faraday rotation. Fig. 6a is similar to Fig. 4c, except that meridional planes from both hemispheres are merged, and colors indicate the arithmetic mean value of the middle frequency F_m in each bin. Dipole field lines at L-shells of 5, 15 and 30 are overplotted in purple color. Fig. 6b is a restructuring of bins with radial distance and northern and southern latitudes. The x-axis is chosen to be logarithmic for showing finer details at smaller radial distances.

Since FREs at low frequencies are clearly outweighing those at higher frequencies (see also Fig. 3c), most of the bins in Fig. 6 contain a mean F_m below ~200 kHz (blue shades). A closer look at Fig. 6b suggests some systematic structuring with dipole L-shell, i.e., F_m seems to be gradually decreasing across the indicated field lines while moving away from Saturn. We will discuss this feature in more detail in Section 4 in terms of the special beaming geometry of auroral X-mode SKR. Inside a radial distance of ~10 R_S, the lower latitude boundary of the region where FREs become visible is gradually shifting from LAT = 20° to

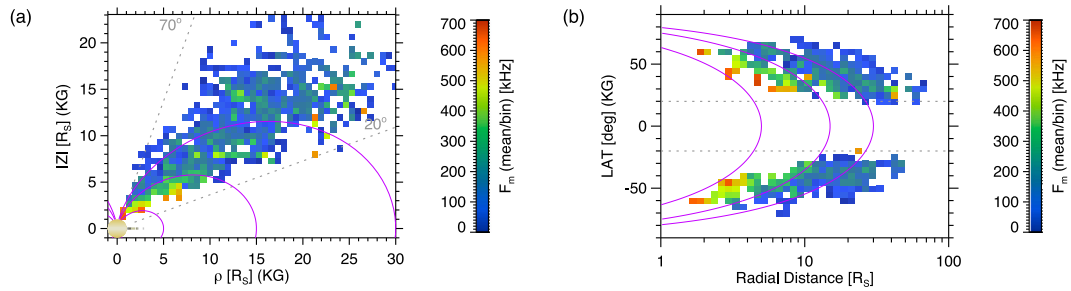

Fig. 6. Binning of the middle frequency F_m of FREs (a) as a function of ρ and $|Z|$ (meridional plane) and (b) as a function of radial distance and latitude (KG coordinates). The mean value of F_m per bin is shown in rainbow colors. Bin sizes are (a) $2/3\,R_S \times 2/3\,R_S$ and (b) $\ln(10)\,0.05\,r\,[R_S] \times 5°$, respectively. Purple lines indicate dipole field lines at L-shells of 5, 15 and 30. (For interpretation of the references to color in this figure legend, the reader is referred to the web version of this article.)

higher values while approaching the planet. This restricts the region of probable density structures, that allow the propagation medium to become birefringent, to a volume of L > 5.

4. Beaming and viewing geometry

In the following we attempt to reconstruct the necessary viewing geometry between the SKR source region and Cassini in order to better understand the observed occurrence distributions of FREs from Section 3. One possible method of analysis for such a task is direction finding (goniopolarimetry), by following a straight ray from the position of Cassini back to the SKR source region. This technique will be utilized in the frame of a case study later on in Section 5. Here, we are going to test a more simple approach first, by assuming a fixed location of the radio source and investigating those rays along which Faraday rotation has been observed. A selection of SKR-rays that belong to FREs is achieved via the meridional distribution of frequencies as presented in Fig. 6a. First, the setup of the model and the choice of relevant parameters will be explained.

As a starting point we assume an auroral magnetic field line from a dipole model at an L-shell of 15. Along this field line, active radio sources (point sources for simplicity) shall emit X-mode SKR at a frequency which closely matches the local electron cyclotron frequency as a consequence of the cyclotron maser mechanism. The beaming pattern of SKR corresponds to that of a hollow cone, with the source being located at the cone's apex, and the cone's wall forming an angle of 50°–75° with respect to the local magnetic field direction (Lamy et al., 2011; Lamy, 2017). These beaming angles relative to the direction of $\mathbf{B_0}$ depend on frequency, and they are relevant for observations made just outside of the immediate source region. Inside the source, the CMI generates wave vectors at perpendicular (~90°) angles to $\mathbf{B_0}$, but these get quickly reduced by refraction and reflection during escape of the radio waves from the source region. Once SKR had left the source region, we assume straight-line propagation for simplicity.

An illustration of this scenario is presented in Fig. 7. The L=15 field line is drawn in purple color, and it is chosen to be in the $[-y, z]$-plane. Three active SKR sources together with their emitting hollow-cone structures are illustrated for frequencies of 20 kHz (blue), 100 kHz (green) and 600 kHz (red), respectively. A projection onto the back wall of the viewing area shows again the three radio sources and their 2D cone structures on the left-hand side. The cones' half-opening angles are chosen to be 75° for 20 kHz, 70° for 100 kHz, and 60° for 600 kHz, respectively (Lamy et al., 2011; Lamy, 2017). For the 100 kHz source, part of the cone's grid is extended to larger radial distances (shown in gray color) for illustrating its orientation in 3D. In order to prevent Fig. 7 from becoming too cluttered, we refrain from plotting extended cone grids for more than one frequency. Also for the sake of clarity, the grid is only plotted at positive x-coordinates. Of course, it is mirroring symmetrically to the negative x-hemisphere as well.

In addition to the cone grid, there are segments of rays overplotted in green color for the 100 kHz source. These segments are shown only at positions that, when mapped into the meridional $[\rho, z]$-plane, belong to bins where Faraday rotation was actually observed by Cassini for that specific frequency. Such an approach aims to link the model to the actual observations and enables a selection of only those modeled SKR-rays that are known to have Faraday rotation included. In order to limit the amount of modeled rays to a reasonable number, we set the azimuthal resolution of the cone grid to 6°, so that each source is emitting a total of 60 rays along the circumference of its cone.

The same procedure has been performed for the rays from the 20 kHz source and from the 600 kHz source as well, although corresponding FRE-ray segments are only shown as a projection into the $[x, y]$-plane and into the $[\rho, z]$-plane. For a binning in the meridional plane, we choose a resolution of $0.5 \times 0.5\,R_S$. An accumulation of all ray segments in the $[\rho, z]$-plane from all three source regions is plotted on the right-hand side of the back wall of the viewing area in Fig. 7. The distribution of frequencies inside this plane must yield a similar picture to Fig. 6, except that only three selected frequencies are included here, and there is no mean-per-bin performed. Another difference is that Fig. 6 is established from all active SKR sources across the entire longitudinal range, whereas the distribution on the back wall of Fig. 7 is modeled with one active field line at a fixed longitude. We will discuss implications of this simplified approach below.

As a next step, the azimuthal distribution of ray segments is going to be analyzed in more detail. It results from a combination of the setup of the model (fixed azimuth of source field line; given geometry of emitting hollow cone) and observational constraints, i.e., the selection of ray segments with regard to the observed distribution of FREs in the meridional $[\rho, z]$-plane. A projection of corresponding ray segments into the $[x, y]$-plane leads to the following conclusions:

- As can be seen in the $[x, y]$-plane of Fig. 7, most FRE-ray segments from the three selected frequencies have azimuthal separation angles of ~80°–120° to the meridional plane containing the source field line. This is also illustrated by a histogram of occurrences which is overplotted in the $[x, y]$-plane in gray color. It shows the number of ray segments belonging to FREs as a function of azimuth (bin size = 10°). If the assumptions for our beaming model are correct, this suggests that most FREs are observed when the source field line and Cassini are approximately in quadrature to each other. Some rays, especially those from the 100 kHz source (green), can experience Faraday rotation while propagating across the auroral oval of Saturn into the opposite y-hemisphere. On the other hand, Faraday rotation is almost absent in SKR that is beamed along the same meridional plane which also contains the source field line (along -y-direction in this example).
- In principle, a symmetric pattern of emission also exists in the negative x-hemisphere, although not shown here for the sake of clarity. Furthermore, the static model presented here does not include aspects of rotation. A source field line rotating with the planet would simply move the entire emission pattern in azimuthal direction. However, the emission pattern itself remains

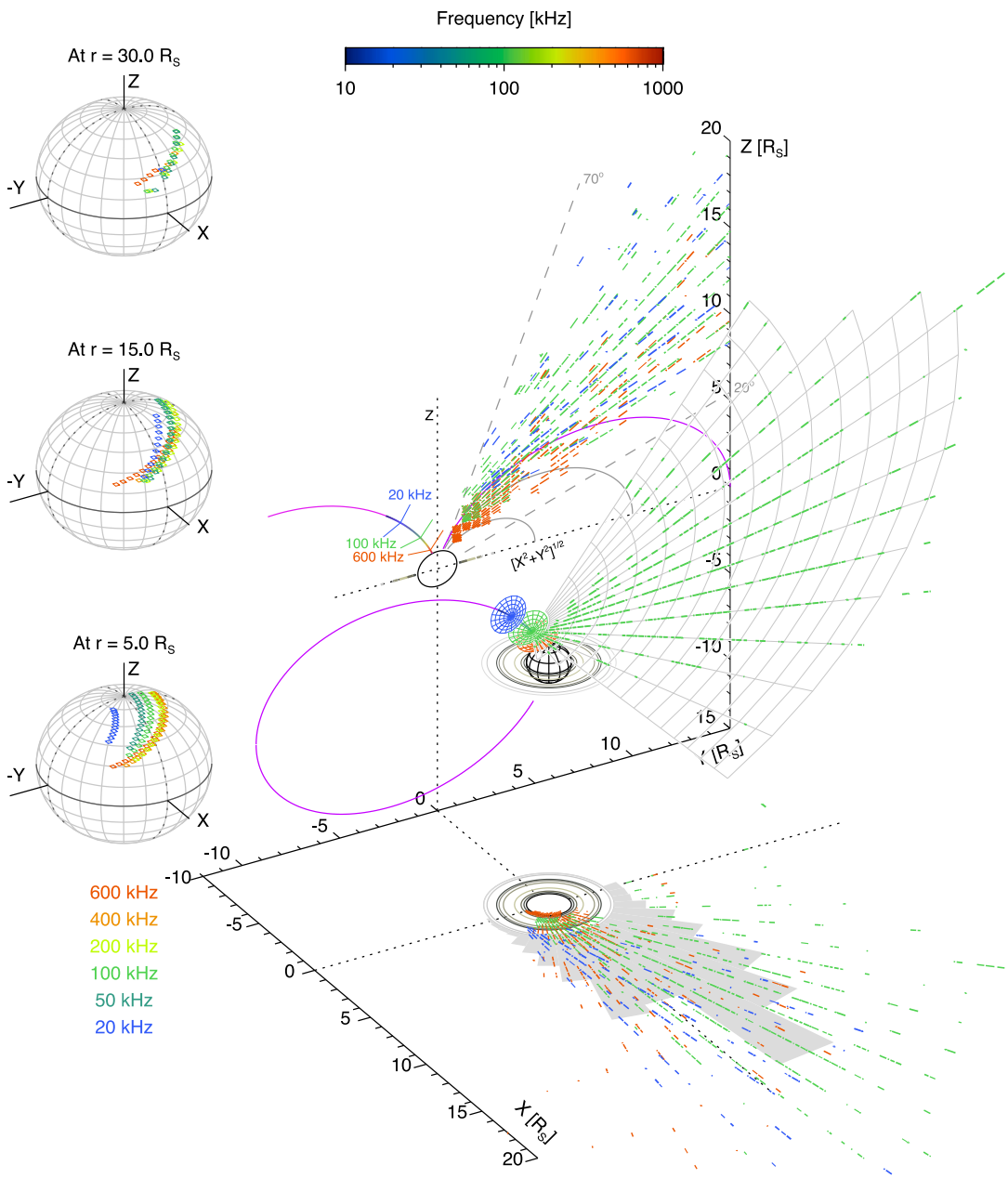

Fig. 7. Illustration of the beaming characteristics of SKR-rays that include Faraday rotation. Emission cones are drawn on a common dipole field line (purple) for three SKR frequencies: 20 kHz (blue), 100 kHz (green) and 600 kHz (red). Part of the emission cone from the 100 kHz source is extended with a 3D-grid (gray). Segments of rays that fall into bins in the meridional $[\rho, z]$-plane (see back wall of viewing area) where Faraday rotation is actually observed by Cassini, are highlighted with respective colors. On the left-hand side, rays including Faraday rotation are intersected with spheres of three given sizes ($r = 5, 15$ and $30\ R_S$) around Saturn, and the intersecting points are shown with diamond symbols. (for more details see text). (For interpretation of the references to color in this figure legend, the reader is referred to the web version of this article.)

unchanged. The same is true for an inclusion of many source field lines that are distributed across a certain longitudinal range. One would simply see a superposition of identical patterns, each corresponding to the one shown in the $[x, y]$-plane of Fig. 7.

- So far, the azimuthal direction in this model is treated exclusively in terms of separation angle between the source field line and the observer. However, a comparison of Fig. 7 with Fig. 4 motivates an interpretation of azimuth as Local-Time coordinate, for which the axes shall coincide with the main axes of the non-spinning KG-system. Then, the source field line from Fig. 7 is pointing toward LT 6:00 ($-y$-axis in the KG system). SKR emitted from this field line will have Faraday fringes included if observed from high latitudes ($> 20°$) in the noon/afternoon sector. This is exactly the pattern of occurrence distribution from Fig. 4d,e. Such similarities suggest that SKR source regions from the dawn side of Saturn are predominantly those which are responsible for Faraday rotation events. The fact that FREs are primarily observed on the dayside is justification for not drawing a symmetric fan of rays in the negative x-hemisphere of Fig. 7, which would be the nightside in the KG-system. There seems to be a strong tendency for plasma especially on the morning side, and at high latitudes, to introduce Faraday rotation into SKR. Moreover, this tendency is enhanced for rays that are beamed toward the dayside, but is less frequently observed for rays that are beamed toward the nightside.

Hollow cone grids for SKR rays belonging to different frequencies, as drawn in Fig. 7, have different orientations in space due to the following reasons: (1) inclination of the field line at the corresponding

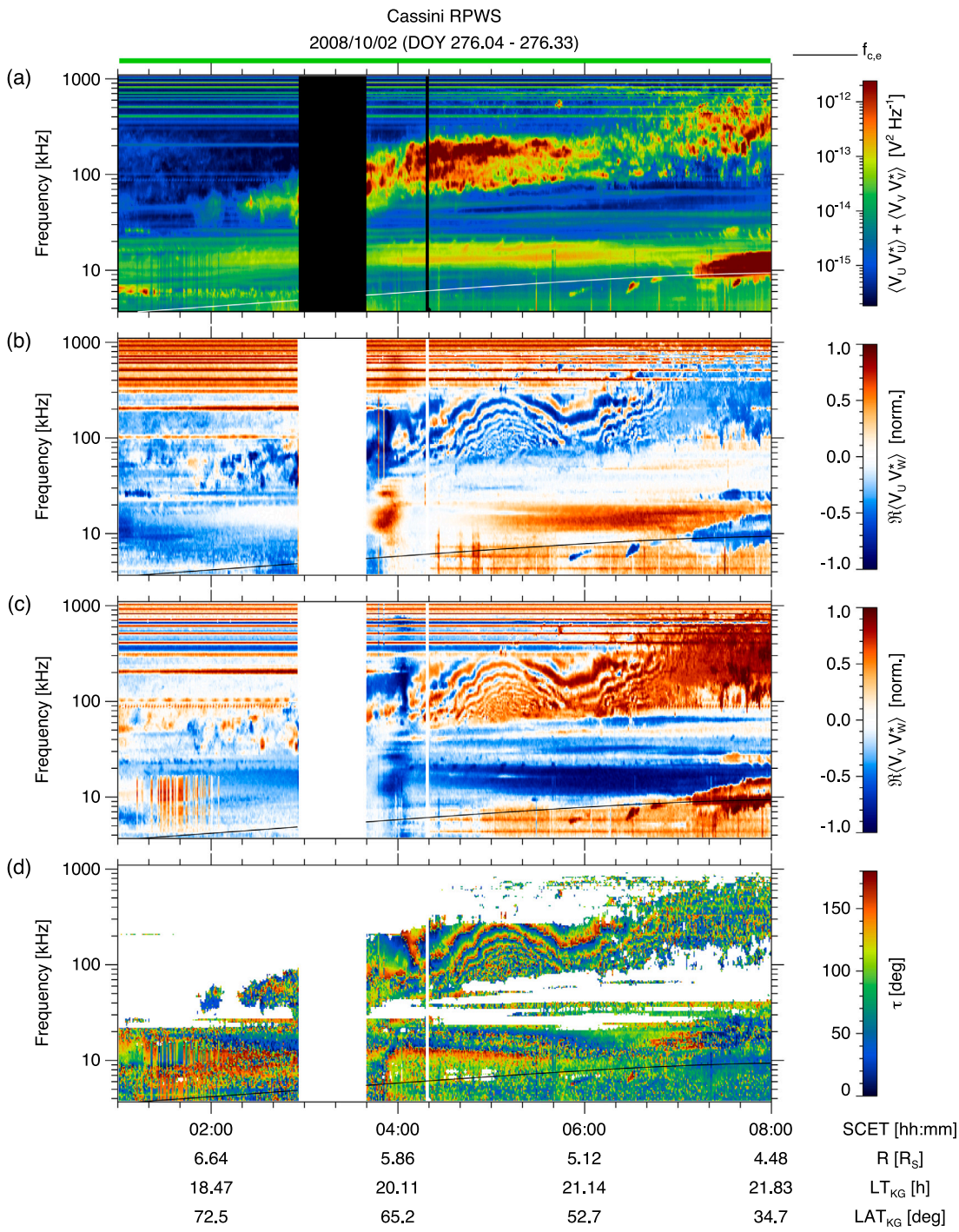

Fig. 8. (a) Sum of auto-power spectral densities in the u and v antennas, real part of normalized cross-spectral power between (b) the u and w antennas and (c) the v and w antennas, and (d) the tilt angle τ between the x-axis of the wave-frame and the semi-major axis of the polarization ellipse from Cassini/RPWS measurements on October 2, 2008. The local f_c is indicated by a white (a) or black (b–d) curve.

source region and (2) opening angle for the corresponding emission cone. Depending on the relative position of the observer with respect to the source field line, one should see a different selection of frequencies able to reach the observer. This situation is illustrated by three spheres on the left-hand side of Fig. 7. These spheres show intersecting points of rays of six selected frequencies with a spherical surface around Saturn at certain radial distances: 5, 15 and 30 R_S. The six color-coded frequencies are 20 kHz (blue color; 75° beaming angle), 50 kHz (dark green; 75°), 100 kHz (light green; 70°), 200 kHz (yellow; 70°), 400 kHz (orange; 65°), and 600 kHz (red; 60°). Colored diamond symbols mark the points of intersection, and they are only shown if FREs at the corresponding frequency are observed at least up to the radial distance of the sphere's surface. One can see that close to Saturn, at $r = 5\,R_S$, FREs below 100 kHz are well separated in space, especially with regard to longitude. This makes it very unlikely for Cassini to observe Faraday fringes across a broader frequency range below 100 kHz when the spacecraft is so close to the planet. At a larger radial distance ($r = 15\,R_S$), the colored spots tend to merge, i.e., FREs over a wider range of frequencies are observable at similar latitudes and azimuthal separations from the source field line. High frequency FREs are still

visible at $r = 15\,R_S$, but they are starting to become outweighed by medium and low frequency FREs. This reflects the decrease seen in average F_m with distance in Fig. 6 which seems to be a consequence of the beaming geometry and the requirement of ray propagation through a plasma that is conditioned for Faraday rotation. Eventually, at even greater radial distances of $r = 30\,R_S$, FREs at medium frequencies of $\sim 50 < f < 200\,\mathrm{kHz}$ do prevail.

5. Goniopolarimetric analysis — a case study

Faraday rotation is not only found in RPWS 2-antenna mode data, as already demonstrated in Fig. 2, but also when signals from all three antennas are processed simultaneously. From the 611 identified FREs, 383 were recorded in 2-antenna mode, 113 in 3-antenna mode, and 115 are a mixture of both modes. The 3-antenna mode sometimes provides less spectral resolution, but it allows for a determination of the direction of incidence of the radiation as well as a determination of all four 2D Stokes parameters by using an analytical inversion technique (Cecconi and Zarka, 2005). It should be noted that the inversion used here is operating in a slightly different coordinate system than proposed in Cecconi and Zarka (2005), but we verified that our results agree with the N3b data set which is directly accessible from the Meudon data server (Cecconi et al., 2017b).

Fig. 8 is an example of Faraday rotation found in 3-antenna mode observations on October 2, 2008. Fringe patterns are visible in the real parts $\Re\langle V_u V_w^*\rangle$ (Fig. 8b) and $\Re\langle V_v V_w^*\rangle$ (Fig. 8c) from cross-correlations between antennas u-w and v-w, respectively. Fig. 8d is a spectrum of the rotation angle τ which is computed after Eq. (3). Values for noise below a threshold of $2 \times 10^{-15}\,\mathrm{V^2\,Hz^{-1}}$ are colored in white. τ specifies the angle between the semi-major axis of the polarization ellipse and the x-axis of the wave-frame. The latter is defined here as the projection of the rotation axis of Saturn into the $[x, y]$-plane of the wave-frame ($+x$ pointing North). In general, the choice of the x-axis direction is arbitrary, but it should be stable over time, e.g., it should not be fixed to the spacecraft reference frame while Cassini is doing attitude maneuvers. A closer inspection of the Faraday fringe pattern in Fig. 8d between 4:00 and 7:00 SCET and 50–300 kHz reveals that τ is repetitively decreasing through all angles between 180° and 0° as one scans through the spectrum from low frequencies to high frequencies. This is expected according to Eq. (2) for an observation in the northern hemisphere of Saturn, where SKR rays propagate ~along the direction of magnetic field lines toward the Cassini spacecraft, i.e., $\theta_k < 90°$ ($\cos\theta_k > 0$). In the southern hemisphere, $90° < \theta_k < 180°$ ($\cos\theta_k < 0$), which yields an increasing θ_F with increasing frequency.

The direction of incidence of SKR-rays at the antenna system of Cassini can be used to trace the rays back toward their supposed source regions (Cecconi et al., 2009; Lamy et al., 2009, 2010). As a first approximation, straight ray propagation is assumed. The source region is located where the wave frequency matches the local electron cyclotron frequency along the straight ray path. Fig. 9 illustrates ray tracing results from a 20-minute window in time around 06:00 SCET (05:50–06:10 SCET) and from a limited frequency bandwidth of 80–280 kHz, i.e., from a spectral area in Fig. 8 that contains Faraday rotation in SKR. From the 1131 available spectral points, ray tracing is performed with only 74 points that fulfill the following quality criteria: degree of polarization $D_p > 0.8$ (for definition of D_p see e.g. Taubenschuss and Santolík, 2019), $S > 15$ dB above background noise level, $\beta > 30°$ and $\gamma < 0.05$. β specifies the minimum angle of incidence between the ray and all three antenna planes. This angle should be above 30° to ensure the necessary accuracy of derived Stokes parameters (Cecconi and Zarka, 2005). γ specifies the relative difference between two successive auto-correlation signals at the w-antenna, once measured in combination with $\langle V_u V_u^*\rangle$, and immediately afterwards in combination with $\langle V_v V_v^*\rangle$. Thus, $\gamma = |\langle V_w V_w^*\rangle_{uw} - \langle V_w V_w^*\rangle_{vw}|/\langle V_w V_w^*\rangle_{uw}$. A relative difference of less than 5% ensures a temporally stable radio source at a given time and frequency, at least during the time it takes the receiver to switch between different antennas (45–2000 ms (Gurnett et al., 2004)).

All 74 confirmed source regions are plotted from the viewpoint of Cassini with colored plus symbols in Fig. 9a. Colors represent frequency, and sources exhibit a distinct distribution with frequency along auroral magnetic field lines. Cassini is positioned at high northern latitudes of ~52° and is looking down toward Saturn and its rings. A projection of SKR sources along the magnetic field lines onto the surface of Saturn (1-bar level) is plotted in Fig. 9b. As can be seen, footprints of source field lines are grouped around LT ~ 16:00, and they are positioned approximately in quadrature with respect to the direction toward Cassini, which is indicated by a pink dashed line (Cassini at LT ~21:00). This confirms the picture which has been modeled in Section 4, where SKR rays that are beamed from Saturn's limb toward the observer are those which are likely to be affected by Faraday rotation. However, the ray tracing example presented here belongs to a statistically rare case of FREs being observed by Cassini on the nightside of Saturn (LT ~ 21:00).

The angle between the straight ray path and the local magnetic field direction is displayed in Fig. 9c. Technically, this angle describes the deviation of the group velocity vector $\mathbf{v_G}$ from the local magnetic field vector $\mathbf{B_0}$. However, if we assume a cold plasma, this angle should be very close to θ_k, i.e., the angle between the wave vector $\mathbf{k}$ and $\mathbf{B_0}$. SKR rays start at oblique angles of 40°–80° to $\mathbf{B_0}$ at the source region, but they are becoming gradually more parallel while propagating toward Cassini. Conditions of quasi-parallel propagation are those that favor Faraday rotation to occur along the way.

We do not include an analysis of the SKR dispersion relation because this would require a detailed knowledge of the configuration of plasma along the ray path. Unfortunately, there are no large-scale plasma density models available for the high latitude magnetosphere of Saturn. Distinct features in the density distribution would have to be included in order to accurately model the process of mode splitting and to reproduce observed fringe patterns from modeled phase differences between the R-mode and the L-mode. This is beyond the scope of this study.

A comparison of the measured tilt τ of the polarization ellipse to Eq. (2) provides an estimate of the plasma density along the ray path. The data are taken from the same 20-minute interval as before, but the number of rays is increased to 228 by loosening the constraints on S, D_p and γ, allowing for $S > 5$ dB above background, $D_p > 0.5$ and $\gamma < 0.10$.

At first, the integral expression in Eq. (2) is substituted with parameter χ, yielding

$$\theta_F = \frac{23648}{f^2}\,\chi\,. \tag{6}$$

All constants in front of the integral are summarized in the number 23648, which has the unit $[\mathrm{m^2\,T^{-1}\,s^{-2}}]$. Parameter χ has to be adjusted for matching θ_F from Eq. (6) with the observed τ. Observed τ-values from the 20-minute window around 06:00 SCET are plotted in Fig. 10a with diamond symbols. For the sake of clarity, only a limited subset consisting of five selected time-steps, i.e., spectrum columns, is shown (from a total of 35 time-steps, with $\Delta t = 32\,\mathrm{s}$). Time is indicated by rainbow colors. In order to increase the number of τ-values per time-step, we also add data from the directly preceding and succeeding time-steps to the central time-step (3-point data selection window sliding across spectrum columns).

The dashed lines in Fig. 10a are from a least-squares fit of the form $\tau = c_0 + c_1/f^2$. Coefficient c_0 serves for adjusting the zero-level. It represents θ_{F0} at $f \to \infty$, i.e., it can be interpreted as the original orientation angle of the polarization ellipse before the wave enters the Faraday rotation medium. The critical assumptions involved with this interpretation were discussed in Section 1. Note that all τ-values shown in Fig. 10a have c_0 already subtracted. Furthermore, jumps in τ from 0° back to 180° have been removed. Thus, the c_0-normalized fits $\tau = c_1/f^2$

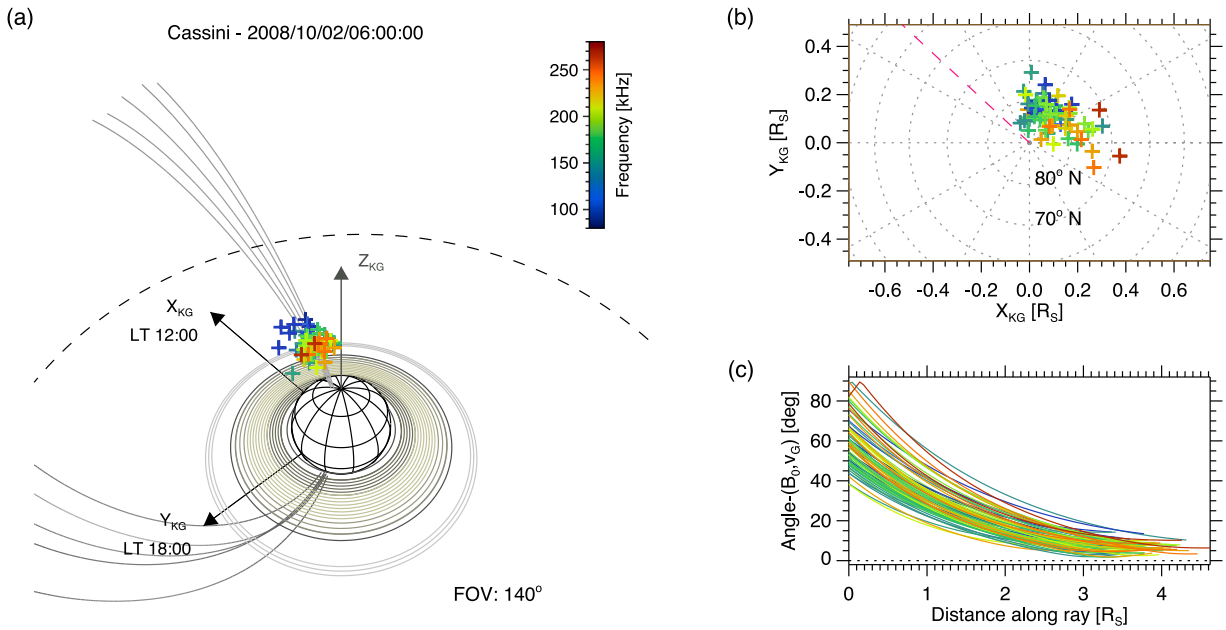

Fig. 9. (a) View from the Cassini spacecraft of Saturn, its rings, the equatorial magnetopause (dashed line) for average solar wind conditions (Kanani et al., 2010), identified SKR sources from ray tracing (plus symbols) and a cluster of dipole field lines running through the center of the group of SKR sources. Rainbow colors indicate SKR frequency. (b) Projection of SKR sources onto Saturn's surface ($r = 60268$ km) along dipole field lines, and (c) the angle between SKR rays (direction of group velocity $\mathbf{v_G}$) and the local $\mathbf{B_0}$ during straight-line propagation from the source point toward Cassini. (For interpretation of the references to color in this figure legend, the reader is referred to the web version of this article.)

can be directly compared to Eq. (6) for estimating the value of the integral from $c_1 = 23648\,\chi$. The integral χ from each fit, i.e., from each time-step, is then used to obtain an estimate for the plasma density n_e as a function of time. The latter can only be separated from the term $B_0 \cos\theta_k$ inside the integral if n_e is replaced by a constant average value $\langle n_e \rangle$ along the ray path, yielding

$$\langle n_e \rangle = \frac{\chi}{\int_{z_1}^{z_2} B_0(z)\,\cos\theta_k\,dz}\,. \tag{7}$$

The bounds of integration $[z_1,\ z_2]$ specify the segment of the ray path along which Faraday rotation is active. Unfortunately, this is unknown without further information on the exact location where mode-splitting is happening and on the dimensions of the birefringent medium between the source and Cassini. For now, we assume that Faraday rotation is initiated just after the ray had left the source region, and that a phase shift between the R-mode and the L-mode is accumulating along the entire ray path until the position of Cassini.

The magnetic field $\mathbf{B_0}$ is modeled with Saturn's dipole, which is a reasonable assumption at radial distances inside $r = 5.1\,\mathrm{R_S}$. The wave normal angle used in the term $\cos\theta_k$ is calculated from the assumption of straight ray propagation through a cold plasma and a dipole magnetic field (see also Fig. 9c). Retrieved values for $\langle n_e \rangle$ from Eq. (7) at each time-step inside the 20-minute window are plotted in Fig. 10c. Densities at the five selected time-steps used for Fig. 10a are indicated with slightly larger diamond symbols. Corresponding standard deviations are indicated by colored vertical lines. These are computed for each $\langle n_e \rangle$-value which is not only an average along the entire ray path but also an average from all included rays, i.e., from all frequency components that contribute to the τ-fit at a specific time-step. The number of τ-values available at each time-step is plotted in Fig. 10b in gray color. Due to our strategy of using a 3-point wide sliding window, there are always more than 10 τ-values available per fit. The root-mean-square (RMS) error for each fit is overplotted with rainbow colors in Fig. 10b. RMS-errors are typically below ~25°, which demonstrates the reliability of computed fits. For the most part, the Faraday fringe pattern seems to be stable enough during the selected time window to yield a congruent estimate for the average plasma density of $\langle n_e \rangle \sim 0.01\,\mathrm{cm^{-3}}$ along all analyzed rays. This value agrees quite well with densities derived from the Cassini Langmuir probe in the magnetodisc at higher latitudes (Morooka et al., 2009). However, densities from the immediate vicinity of the SKR source region and further poleward can also be another order of magnitude lower (down to ~0.001 $\mathrm{cm^{-3}}$) (Lamy et al., 2010, 2018; Gurnett et al., 2010).

Besides the errors discussed above, which result from uncertainties in fitting the observed τ-values and averaging over different rays, a reliable density estimate is also affected by other limitations. On the one hand, the accuracy with which τ can be measured depends on constraints inherent to the goniopolarimetric analysis technique. On the other hand, errors do result from wrong assumptions regarding the integration distance z in Eq. (7), unless one can rely on a detailed model for the distribution of plasma along the ray path. For comparison, we also compute $\langle n_e \rangle$ based on a scenario in which the denominator in Eq. (7) is not integrated along the entire ray path but z_1 is shifted to a point where the rays penetrate a hypothetical plasma boundary at a radial distance of $3\,\mathrm{R_S}$, i.e., Faraday rotation starts at approximately halfway between the individual sources and Cassini. This excludes the immediate vicinity of the source regions where the rays are far from being quasi-parallel to $\mathbf{B_0}$, and it allows for similar propagation distances through the birefringent medium for individual rays so that a regular fringe pattern can develop across a broad range of frequencies. As a consequence, retrieved densities are a bit higher, i.e., the profile from Fig. 10c gets shifted upward to values of $\langle n_e \rangle \sim 0.03\,\mathrm{cm^{-3}}$. This increase is due to a shorter path segment over which an average of n_e is performed, and due to smaller values of B_0 at larger radial distances. Both effects excel a minor decrease of $\langle n_e \rangle$ due to larger values for $\cos\theta_k$. For comparison, if we reset z_1 to the source region and assume a constant $\cos\theta_k = 1$ for all rays, then $\langle n_e \rangle$ is decreasing slightly from ~0.01 $\mathrm{cm^{-3}}$ to ~0.007 $\mathrm{cm^{-3}}$.

A stable density profile as shown in Fig. 10c indicates that the majority of SKR rays take approximately the same path through the birefringent medium between the SKR source region and the position of Cassini (at $r \sim 5.1\,\mathrm{R_S}$). If this would not be the case, we would see larger RMS-errors from the fits and stronger fluctuations in derived densities. When looking at time periods of several tens of minutes or

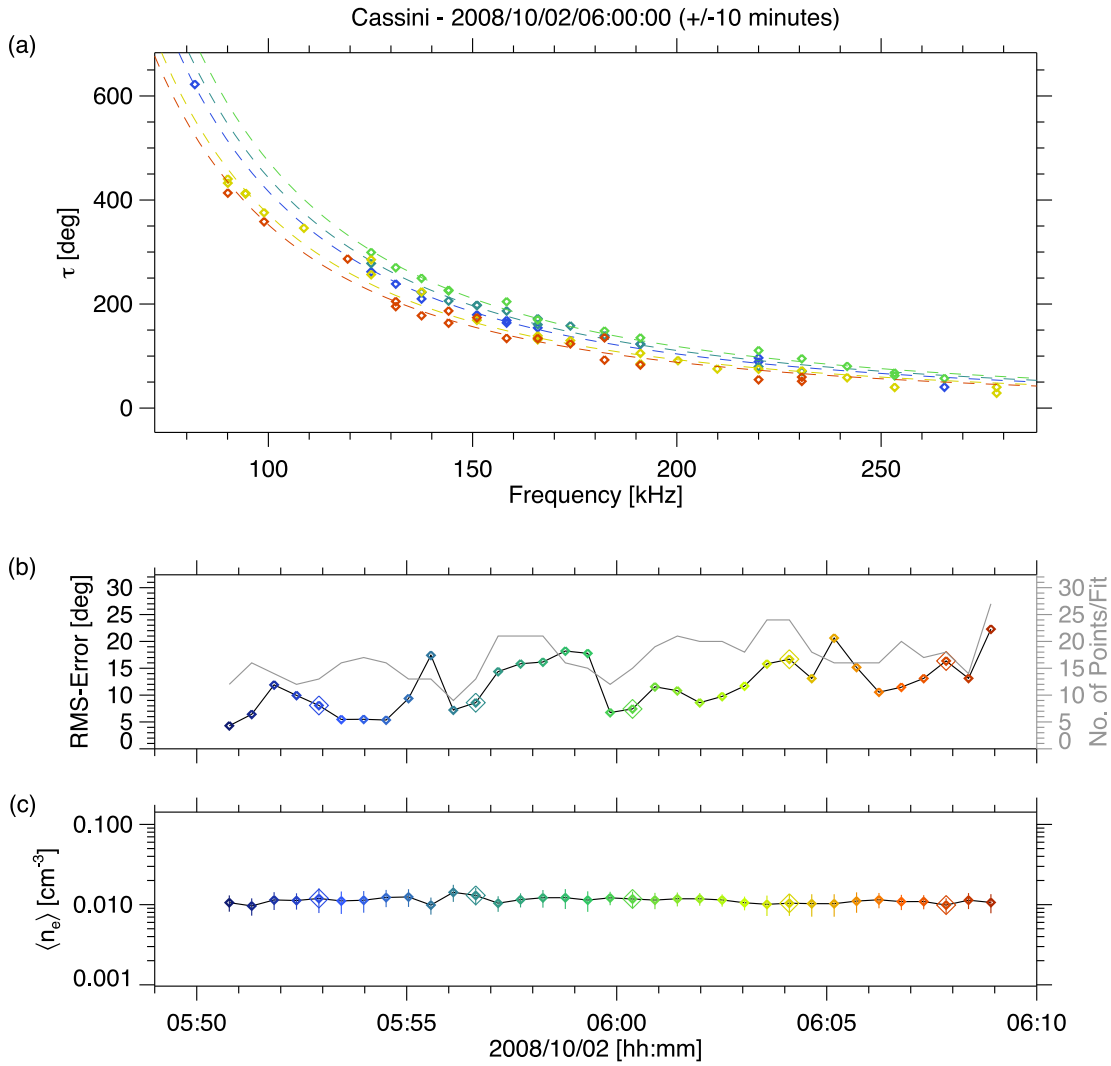

Fig. 10. (a) Fitting of measured Faraday rotation angles τ (diamond symbols) to a theoretical θ_F (dashed lines; see Eq. (6)) between 80–280 kHz and during 05:50–06:10 SCET on October 2, 2008. Rainbow colors indicate time, and fits are shown for five selected time-steps. (b) The root-mean-square error (in rainbow colors) and the number of available τ-values (gray) for the fits at all 35 time-steps. (c) Inferred average plasma densities as a function of time. Short vertical lines indicate the standard deviations when averaging $\langle n_e \rangle$-estimates from all rays belonging to the same time-step. (For interpretation of the references to color in this figure legend, the reader is referred to the web version of this article.)

hours, the contours of τ in Fig. 8d are modulated considerably as the geometry between the SKR source regions and the observer is changing. This is either due to the movement of the spacecraft, or a corotation of source field lines with Saturn, or a drift motion of energetic electrons that are injected into the auroral region, causing the rays to take slightly different paths to Cassini, thereby crossing media with different birefringent properties.

6. Discussion and conclusions

All Cassini RPWS/HFR recordings from the entire orbital phase of the mission (2004–2017) have been examined for the Faraday rotation effect in Saturn kilometric radiation. The final number of 611 confirmed Faraday rotation events (FREs) is the basis for an extensive statistical analysis. The latter, together with results from direction finding of one particular event, leads to the following picture. Faraday rotation is observed mainly in low-frequency SKR (below ~200 kHz) from source regions on auroral magnetic field lines that are preferentially located in the dawn sector. Rays which become affected by Faraday rotation are those which are beamed toward higher magnetic latitudes (> 20°) at an angle of approximately 90° or larger relative to the meridian of the source field line. Furthermore, rays escaping toward the dayside are more likely to include Faraday rotation than those which escape toward the nightside. Along these special beaming directions, the plasma medium allows SKR to remain elliptically polarized and provides four essential ingredients which are necessary for Faraday rotation: (1) a distinct plasma inhomogeneity, e.g., a sharp density gradient, which causes a splitting of the original X-mode (or O-mode) SKR into a RH-circularly polarized R-mode and a LH-circularly polarized L-mode; (2) sufficiently different refractive indices for both modes so that a relative phase shift can accumulate during propagation; (3) parallel or at least quasi-parallel propagation with respect to the ambient magnetic field so that both modes can remain circularly polarized; (4) similar conditions during propagation for many rays belonging to a broader range of frequencies so that a regular fringe pattern can develop across frequency.

From the observations it is not directly apparent where the regions of Faraday rotation exactly are. The immediate SKR source region can be ruled out because of a violation of $f_{SKR} \gg f_c$ and amplification of SKR with highly oblique wave normal angles. However, the special beaming of SKR toward higher latitudes enables quasi-parallel propagation at relatively close distances to the source (2–3 R_S; see Fig. 9c). The plasma layers which provide strong density gradients for mode-splitting need to be located at closer distances to the source. The outer

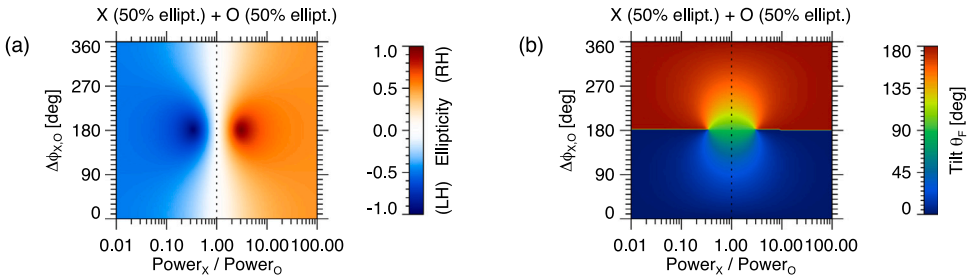

Fig. 11. (a) Ellipticity and (b) rotation angle θ_F of a polarization ellipse that is generated from a superposition of an elliptically polarized X-mode (RH) and an elliptically polarized O-mode (LH) as a function of relative wave power (x-axis) and phase shift (y-axis).

boundary of the Faraday rotation region is defined by the zone of limiting polarization, where the plasma density drops below a critical value, and where mode coupling fixes the elliptical polarization and prevents further Faraday rotation.

In the following, we will discuss two possible scenarios for the occurrence of sharp density gradients which may initiate mode-splitting. The first scenario involves a plasmapause-like boundary layer at high latitudes which has been reported by Gurnett et al. (2010). Field-aligned currents at the transition from open to closed magnetospheric field lines between $8 < L < 15$ (Jasinski et al., 2019) can support a separation of high-density plasma at lower latitudes from low-density plasma at higher latitudes, with abrupt steps in density at the boundary of over three orders of magnitude. The location of this boundary agrees with the fact that Faraday rotation is only observed above 20° latitude and only outside $L > 5$. Stronger density gradients should be located in the dawn sector where associated auroral currents intensify (Hunt et al., 2020). Together with the special SKR beaming geometry discussed in Section 4 this might explain why SKR from the dawn sources preferentially experiences Faraday rotation, resulting in an observational peak of FREs in the noon/afternoon LT-sector.

A shallow modulation of the occurrence rate of FREs with SLS5 longitude, as presented in Fig. 4b, is another indication for a possible link between FREs and the plasmapause-like boundary, which has been found to oscillate in size and position with the rotation period of SKR (Gurnett et al., 2011).

Another hypothesis explaining the formation of strong density gradients at high latitudes has been suggested by Thomsen et al. (2015a). Stretched magnetic flux tubes that reconnect in the nightside tail, either in the frame of the Vasyliunas-cycle (Vasyliunas, 1983) or during plasmoid formation (Jackman et al., 2014), eject their cold and dense plasma into the tail, leaving behind a flux tube that is filled with hot tenuous plasma. These events are also known to be modulated by planetary period oscillations. Strong density gradients at the boundary between reconnected and non-reconnected flux tubes might induce Faraday rotation while SKR is passing through. These structures are found around L-shells of ~10, and they are more similar to a plasmapause as we know it from Earth because they are located entirely inside the region of closed magnetic field lines. However, these flux tubes are unstable to centrifugally driven interchange motion, which makes an appearance of sharp density gradients at a certain location a rather irregular phenomenon (finger-like bulges) (Thomsen and Coates, 2019). The low occurrence rate of FREs reported here (~4% at LAT > 20°) might be attributed to the rarity of situations when SKR is exactly passing through a boundary layer between a mass-loaded and a depleted interchanging flux tube.

Besides Vasyliunas-type reconnection, there is also Dungey-type magnetotail reconnection at Saturn (Dungey, 1961), which can lead to a formation of plasma boundaries between closed magnetospheric flux tubes and reconnected flux tubes that are filled with solar wind plasma from the magnetosheath (Mitchell et al., 2015; Thomsen et al., 2015b). In such a scenario, there should be a clear correlation between the occurrence of FREs and periods of enhanced solar wind activity, e.g., during the impact of a corotating interaction region on Saturn's magnetosphere (see e.g. Bradley et al., 2020 and references therein). A compression of the dayside magnetosphere by the solar wind may lead to significant changes of the configuration of plasma at high latitudes. Although not pursued further in the present study, we keep this in view for a future examination. More statistics including proxies for solar activity, like energetic particle detections from the Cassini MIMI/LEMMS instrument (Roussos et al., 2018), or low-frequency extensions of SKR (Jackman et al., 2009; Reed et al., 2018), as well as correlation studies with time series for normalized SKR intensity can yield further valuable insight.

After mode-splitting, the plasma medium needs to be birefringent for a sufficient distance along the ray path. From the observations alone, it remains unclear along which segment of the ray path a phase shift between R-mode and L-mode is actually accumulated. However, since the Faraday rotation angle θ_F also depends on the strength of the planetary magnetic field B_0, we do expect more significant contributions to θ_F at smaller radial distances, and minor contributions at larger radial distances where B_0 is decreasing rapidly with $1/r^3$. In Sections 4 and 5 , wave propagation was modeled along a straight ray in a dipole magnetic field. These assumptions are very basic ones, and a more complete analysis should involve full 3D ray tracing together with a more realistic model for the background plasma that allows SKR to adapt a limiting polarization (elliptical) at larger radial distances beyond several Saturn radii. A more detailed analysis of single events should definitely be addressed in a future study as well.

Another open question is if a splitting into R-mode and L-mode at a sharp plasma gradient is actually necessary, considering that SKR can be generated in the X-mode and in the O-mode along the same auroral field line. This would provide a scenario of instant superposition, starting already at or very close to the source region. The only requirements that need to be fulfilled are: (a) X-mode and O-mode of identical frequency must propagate along the same ray path and (b) both modes should be of comparable intensity. However, the two modes are not circularly polarized like R and L from Fig. 1. In Fig. 11 the ellipticity and rotation angle θ_F from a superposition of a 50% elliptically polarized X-mode and 50% elliptically polarized O-mode are analyzed. These results are again based on numerical simulations for a superposition of two plane waves. As one can see from Fig. 11b, a smooth rotation through all orientation angles between 0° and 180° is only provided for power ratios that deviate from 1 by less than a factor of ~3. If one mode is much stronger than the other, then Faraday rotation will not be observed. This is most likely the case according to various studies (Cecconi et al., 2009; Lamy et al., 2011, 2018) which found that X-mode radio fluxes are on average 10^2–10^4 times brighter than O-mode fluxes. Furthermore, both modes tend to experience different refraction near the source region which causes their ray paths to diverge, thereby preventing any appearance of Faraday rotation.

A peculiar feature of Fig. 11a are two isolated peaks of enhanced ellipticity near $\Delta\phi_{X,O} = 180°$. We did not investigate this further, but if a scenario of direct superposition of X-mode and O-mode were to be true, one would also have to provide observational evidence for such

a feature in ellipticity. It should be noted that the simulated patterns obtained in Fig. 11 depend strongly on the individual ellipticities of both involved modes and need to be adjusted for each analyzed event.

Finally, we want to emphasize that a derivation of plasma density from Faraday rotation has some limitations. First, only an average density along the ray path can be inferred. The exact distribution of density with distance remains unknown. Second, it is unclear which segment of the ray path actually introduces Faraday rotation into SKR unless there is a clearly defined segment that allows for quasi-parallel propagation in contrast to the rest of the ray path. This becomes important for Faraday rotation events that are observed at large radial distances to Saturn, for which it is unreasonable to assume that the plasma has birefringent properties along the entire ray path, out to a distance of several tens of R_S. These events should be excluded from a density analysis anyway because of angular uncertainties inherent to the method of goniopolarimetry. However, at close vicinity to Saturn, i.e., inside $r \sim 20\,\mathrm{R_S}$, Faraday rotation in SKR can be a useful source of additional information for improving models of plasma density at high magnetic latitudes.

Acknowledgments

The Cassini/RPWS/HFR LESIA/Kronos N2 (level 2) data collection has been produced by B. Cecconi, L. Lamy & P. Zarka, from the Observatoire de Paris/LESIA Cassini-RPWS team, with the support of CNRS and CNES (Cecconi et al., 2017a). Cassini trajectory data are provided by the Cassini RPWS Team page at http://cassini.physics.uiowa.edu/cassini/team/team.html and by the Cassini/RPWS/HFR LESIA/Kronos data repository at https://lesia.obspm.fr/kronos/data/. A list of all identified Faraday rotation events can be accessed at https://doi.org/10.25935/R11G-6J63 (Taubenschuss et al., 2021).

This work has been done partly within the LABEX PLAS@PAR project, and received financial state aid managed by the "Agence Nationale de la Recherche, France", as part of the "Programme d'Investissements d'Avenir" under the reference ANR-11-IDEX-0004-02. U.T., G.F., D.P., J.S., O.S. and H.O.R. acknowledge support from the FWF-GAČR international project, Austria I 4559-N/20-06802L. This research was funded in whole, or in part, by the Austrian Science Fund (FWF) [I 4559-N]. For the purpose of open access, the author has applied a CC BY public copyright license to any Author Accepted Manuscript version arising from this submission. The french co-authors were supported by CNES, France and CNRS/INSU, France national program of planetology and heliophysics.

References

Bittencourt, J.A., 2004. Fundamentals of Plasma Physics. Springer, New York.

Boudjada, M., Lecacheux, A., 1991. Faraday rotation of Jupiter's decametric radiation. Astron. Astrophys. 247, 235–246.

Bradley, T.J., Cowley, S.W.H., Bunce, E.J., Melin, H., Provan, G., Nichols, J.D., Dougherty, M.K., Roussos, E., Krupp, N., Tao, C., Lamy, L., Pryor, W.R., Hunt, G.J., 2020. Saturn's nightside dynamics during Cassini's F ring and proximal orbits: Response to solar wind and planetary period oscillation modulations. J. Geophys. Res. 125, http://dx.doi.org/10.1029/2020JA027907.

Bradley, T.J., Cowley, S.W.H., Provan, G., Hunt, G.J., Bunce, E.J., Wharton, S.J., Alexeev, I.I., Belenkaya, E.S., Kalegaev, V.V., Dougherty, M.K., 2018. Field-aligned currents in Saturn's nightside magnetosphere: subcorotation and planetary period oscillation components during northern spring. J. Geophys. Res. 123, 3602–3636. http://dx.doi.org/10.1029/2017JA024885.

Budden, K.G., 1952. The theory of the limiting polarization of radio waves reflected from the ionosphere. Proc. R. Soc. Lond. Ser. A Math. Phys. Eng. Sci. 215 (1121), 215–233. http://dx.doi.org/10.1098/rspa.1952.0207.

Budden, K.G., 1985. The Propagation of Radio Waves: The Theory of Radio Waves of Low Power in the Ionosphere and Magnetosphere. Cambridge University Press.

Carbary, J.F., Mitchell, D.G., 2013. Periodicities in Saturn's magnetosphere. Rev. Geophys. 51, 1–30. http://dx.doi.org/10.1002/rog.20006.

Cecconi, B., Lamy, L., Zarka, P., 2017a. Cassini/RPWS/HFR LESIA/Kronos N2 Data Collection (Version 1.0) [Data Set]. PADC, http://dx.doi.org/10.25935/XS9J-ND90.

Cecconi, B., Lamy, L., Zarka, P., 2017b. Cassini/RPWS/HFR LESIA/Kronos N3b Data Collection (Version 1.0) [Data Set]. PADC, http://dx.doi.org/10.25935/F8NS-0911.

Cecconi, B., Lamy, L., Zarka, P., Prangé, R., Kurth, W.S., Louarn, P., 2009. Goniopolarimetric study of the revolution 29 perikrone using the Cassini radio and plasma wave science instrument high-frequency radio receiver. J. Geophys. Res. 114 (A03215), http://dx.doi.org/10.1029/2008JA013830.

Cecconi, B., Zarka, P., 2005. Direction finding and antenna calibration through analytical inversion of radio measurements performed using a system of two or three electric dipole antennas on a three-axis stabilized spacecraft. Radio Sci. 40, RS3003. http://dx.doi.org/10.1029/2004RS003070.

Cheng, F.T., Fung, P.C.W., 1977. New approach of studying electromagnetic mode coupling in inhomogeneous magnetized plasma. I: Normal incidence. Astrophys. Space Sci. 49 (2), 367–388. http://dx.doi.org/10.1007/BF00641987.

Dungey, J.W., 1961. Interplanetary magnetic field and the auroral zones. Phys. Rev. Lett. 6, 47–48. http://dx.doi.org/10.1103/PhysRevLett.6.47.

Fischer, G., Cecconi, B., Lamy, L., Ye, S.-Y., Taubenschuss, U., Macher, W., Zarka, P., Kurth, W.S., Gurnett, D.A., 2009. Elliptical polarization of Saturn kilometric radiation observed from high latitudes. J. Geophys. Res. 114 (A08216), http://dx.doi.org/10.1029/2009JA014176.

Fung, P.C.W., Cheng, F.T., 1977. New approach to studying electromagnetic mode coupling in inhomogeneous magnetized plasma. II: Oblique incidence. Astrophys. Space Sci. 50 (2), 361–381. http://dx.doi.org/10.1007/BF00641743.

Goertz, C.K., 1974. Polarization of Jovian decametric radiation. Planet. Space Sci. 22 (11), 1491–1500. http://dx.doi.org/10.1016/0032-0633(74)90014-2.

Gurnett, D.A., Bhattacharjee, A., 2017. Introduction to Plasma Physics: With Space, Laboratory and Astrophysical Applications, second ed. Cambridge University Press, http://dx.doi.org/10.1017/9781139226059.

Gurnett, D.A., Persoon, A.M., Groene, J.B., Kurth, W.S., Morooka, M., Wahlund, J.-E., Nichols, J.D., 2011. The rotation of the plasmapause-like boundary at high latitudes in Saturn's magnetosphere and its relation to the eccentric rotation of the northern and southern auroral ovals. Geophys. Res. Lett. 38, L21203. http://dx.doi.org/10.1029/2011GL049547.

Gurnett, D.A., Persoon, A.M., Kopf, A.J., Kurth, W.S., Morooka, M.W., Wahlund, J.-E., Khurana, K.K., Dougherty, M.K., Mitchell, D.G., Krimigis, S.M., Krupp, N., 2010. A plasmapause-like density boundary at high latitudes in Saturn's magnetosphere. Geophys. Res. Lett. 37, L16806. http://dx.doi.org/10.1029/2010GL044466.

Gurnett, D.A., et al., 2004. The Cassini radio and plasma wave investigation. Space Sci. Rev. 114, 395–463. http://dx.doi.org/10.1007/s11214-004-1434-0.

Hayes, M.G.W., 1971. Theory of the limiting polarization of radio waves emerging obliquely from the ionosphere. Proc. R. Soc. Lond. A. 324 (1558), 369–390. http://dx.doi.org/10.1098/rspa.1971.0145.

Hunt, G.J., Bunce, E.J., Cao, H., Cowley, S.W.H., Dougherty, M.K., Provan, G., Southwood, D.J., 2020. Saturn's auroral field-aligned currents: Observations from the northern hemisphere dawn sector during Cassini's proximal orbits. J. Geophys. Res. 125, http://dx.doi.org/10.1029/2019JA027683.

Hunt, G.J., Provan, G., Bunce, E.J., Cowley, S.W.H., Dougherty, M.K., Southwood, D.J., 2018. Field-aligned currents in Saturn's magnetosphere: Observations from the F-ring orbits. J. Geophys. Res. 123, 3806–3821. http://dx.doi.org/10.1029/2017JA025067.

Jackman, C.M., Lamy, L., Freeman, M.P., Zarka, P., Cecconi, B., Kurth, W.S., Cowley, S.W.H., Dougherty, M.K., 2009. On the character and distribution of lower-frequency radio emissions at Saturn and their relationship to substorm-like events. J. Geophys. Res. 114, A08211. http://dx.doi.org/10.1029/2008JA013997.

Jackman, C.M., Slavin, J.A., Kivelson, M.G., Southwood, D.J., Achilleos, N., Thomsen, M.F., DiBraccio, G.A., Eastwood, J.P., Freeman, M.P., Dougherty, M.K., Vogt, M.F., 2014. Saturn's dynamic magnetotail: A comprehensive magnetic field and plasma survey of plasmoids and traveling compression regions and their role in global magnetospheric dynamics. J. Geophys. Res. 119, 5465–5494. http://dx.doi.org/10.1002/2013JA019388.

Jasinski, J.M., Arridge, C.S., Bader, A., Smith, A.W., Felici, M., Kinrade, J., Coates, A.J., Jones, G.H., Nordheim, A.T., Gilbert, L., Azari, A.R., Badman, S.V., Provan, G., Sergis, N., Murphy, N., 2019. Saturn's open-closed field line boundary: A Cassini electron survey at Saturn's magnetosphere. J. Geophys. Res. 124, 10018–10035. http://dx.doi.org/10.1029/2019JA027090.

Kaiser, M.L., Desch, M.D., Warwick, J.W., Pearce, J.B., 1980. Voyager detection of nonthermal radio emission from Saturn. Science 209, 1238–1240. http://dx.doi.org/10.1126/science.209.4462.1238.

Kanani, S.J., Arridge, C.S., Jones, G.H., Fazakerley, A.N., McAndrews, H.J., Sergis, N., Krimigis, S.M., Dougherty, M.K., Coates, A.J., Young, D.T., Hansen, K.C., Krupp, N., 2010. A new form of Saturn's magnetopause using a dynamic pressure balance model, based on in situ, multi-instrument Cassini measurements. J. Geophys. Res. 115, A06207. http://dx.doi.org/10.1029/2009JA014262.

Kimura, T., Lamy, L., Tao, C., Badman, S.V., Kasahara, S., Cecconi, B., Zarka, P., Morioka, A., Miyoshi, Y., Maruno, D., Kasaba, Y., Fujimoto, M., 2013. Long-term modulations of Saturn's auroral radio emissions by the solar wind and seasonal variations controlled by the solar ultraviolet flux. J. Geophys. Res. 118, 7019–7035. http://dx.doi.org/10.1002/2013JA018833.

Kurth, W.S., Gurnett, D.A., Clarke, J.T., Zarka, P., Desch, M.D., Kaiser, M.L., Cecconi, B., Lecacheux, A., Farrell, W.M., Galopeau, P., Gérard, J.-C., Grodent, D., Prangé, R., Dougherty, M.K., Crary, F.J., 2005. An Earth-like correspondence between Saturn's auroral features and radio emission. Nature 433, 722–725. http://dx.doi.org/10.1038/nature03334.

Kurth, W.S., Gurnett, D.A., Menietti, J.D., Mutel, R.L., Kivelson, M.G., Bunce, E.J., Cowley, S.W.H., Talboys, D.L., Dougherty, M.K., Arridge, C., Coates, A., Grimald, S., Lamy, L., Zarka, P., Cecconi, B., Schippers, P., André, N., Louarn, P., Mitchell, D., Leisner, J., Morooka, M., 2011. A close encounter with a Saturn kilometric radiation source region. In: Rucker, H.O., Kurth, W.S., Louarn, P., Fischer, G. (Eds.), Proceedings of the 7th International Workshop on Planetary, Solar and Heliospheric Radio Emissions (PRE VII), held at Graz, Austria, September (2010) 15-17. Austrian Academy of Sciences Press, Vienna, pp. 75–85.

Ladreiter, H.P., Litvinenko, G., Boudjada, M.Y., Rucker, H.O., 1995. Faraday rotation in Jupiter's decametric radio emission used for remote sensing of the terrestrial ionosphere and the emission's source region at Jupiter. Planet. Space Sci. 43, 12. http://dx.doi.org/10.1016/0032-0633(95)00058-5.

Lamy, L., 2017. The Saturnian kilometric radiation before the Cassini grand finale, Planetary Radio Emissions VIII. In: Fischer, G., Mann, G., Panchenko, M., Zarka, P. (Eds.), Proceedings of the 8th International Workshop Held at Seggauberg, Austria, October (2016) 25-27. Austrian Academy of Sciences Press, Vienna, pp. 171–190. http://dx.doi.org/10.1553/PRE8s171.

Lamy, L., Cecconi, B., Prangé, R., Zarka, P., Nichols, J.D., Clarke, J.T., 2009. An auroral oval at the footprint of Saturn's kilometric radio sources, colocated with the UV aurorae. J. Geophys. Res. 114, A10212. http://dx.doi.org/10.1029/2009JA014401.

Lamy, L., Cecconi, B., Zarka, P., Canu, P., Schippers, P., Kurth, W.S., Mutel, R.L., Gurnett, D.A., Menietti, D., Louarn, P., 2011. Emission and propagation of Saturn kilometric radiation: Magnetoionic modes, beaming pattern, and polarization state. J. Geophys. Res. 116, A04212. http://dx.doi.org/10.1029/2010JA016195.

Lamy, L., Prangé, R., Pryor, W., Gustin, J., Badman, S.V., Melin, H., Stallard, T., Mitchell, D.-G., Brandt, P.C., 2013. Multispectral simultaneous diagnosis of Saturn's aurorae throughout a planetary rotation. J. Geophys. Res. 118, 4817–4843. http://dx.doi.org/10.1002/jgra.50404.

Lamy, L., Schippers, P., Zarka, P., Cecconi, B., Arridge, C.S., Dougherty, M.K., Louarn, P., André, N., Kurth, W.S., Mutel, R.L., Gurnett, D.A., Coates, A.J., 2010. Properties of Saturn kilometric radiation measured within its source region. Geophys. Res. Lett. 37, L12104. http://dx.doi.org/10.1029/2010GL043415.

Lamy, L., Zarka, P., Cecconi, B., Prangé, R., Kurth, W.S., Gurnett, D.A., 2008. Saturn kilometric radiation: Average and statistical properties. J. Geophys. Res. 113, A07201. http://dx.doi.org/10.1029/2007JA012900.

Lamy, L., Zarka, P., Cecconi, B., Prangé, R., Kurth, W.S., Hospodarsky, G., Persoon, A., Morooka, M., Wahlund, J.-E., Hunt, G.J., 2018. The low-frequency source of Saturn's kilometric radiation. Science 362 (6410), aat2027. http://dx.doi.org/10.1126/science.aat2027.

Lecacheux, A., 2011. On SKR and Saturn Auroras Relationship. American Geophysical Union, Fall Meeting 2011, abstract id.SM13F-05.

Lecacheux, A., Boischot, A., Boudjada, M.Y., Dulk, G.A., 1991. Spectra and complete polarization state of two, Io-related, radio storms from Jupiter. Astron. Astrophys. 251, 339–348.

Menietti, J.D., Mutel, R.L., Schippers, P., Ye, S.-Y., Gurnett, D.A., Lamy, L., 2011. Analysis of Saturn kilometric radiation near a source center. J. Geophys. Res. 116, A12222. http://dx.doi.org/10.1029/2011JA017056.

Mitchell, D.G., Brandt, P.C., Carbary, J.F., Kurth, W.S., Krimigis, S.M., Paranicas, C., et al., 2015. Injection, interchange, and reconnection. In: Keiling, A., Jackman, C.M., Delamere, P.A. (Eds.), Energetic Particle Observations in Saturn's Magnetosphere, Magnetotails in the Solar System. In: Geophysical Monograph Series, vol. 207, 19, Wiley, Washington, DC, pp. 327–343. http://dx.doi.org/10.1002/9781118842324.ch19.

Morooka, M.W., Modolo, R., Wahlund, J.-E., André, M., Eriksson, A.I., Persoon, A.M., Gurnett, D.A., Kurth, W.S., Coates, A.J., Lewis, G.R., Khurana, K.K., Dougherty, M., 2009. The electron density of Saturn's magnetosphere. Ann. Geophys. 27, 2971–2991. http://dx.doi.org/10.5194/angeo-27-2971-2009.

Mutel, R.L., Menietti, J.D., Gurnett, D.A., Kurth, W., Schippers, P., Lynch, C., Lamy, L., Arridge, C., Cecconi, B., 2010. CMI growth rates for Saturnian kilometric radiation. Geophys. Res. Lett. 37, L19105. http://dx.doi.org/10.1029/2010GL044940.

Nakamura, Y., Kasaba, Y., Kimura, T., Lamy, L., Cecconi, B., Fischer, G., Sasaki, A., Tao, C., Tsuchiya, F., Misawa, H., Kumamoto, A., Morioka, A., 2019. Seasonal variation of north-south asymmetry in the intensity of Saturn kilometric radiation from 2004 to 2017. Planet. Space Sci. 178, 104711. http://dx.doi.org/10.1016/j.pss.2019.104711.

Oberoi, D., Lonsdale, C.J., 2012. Media responsible for Faraday rotation: A review. Radio Sci. 47, RS0K08. http://dx.doi.org/10.1029/2012RS004992.

Reed, J.J., Jackman, C.M., Lamy, L., Kurth, W.S., Whiter, D.K., 2018. Low-frequency extensions of the Saturn kilometric radiation as a proxy for magnetospheric dynamics. J. Geophys. Res. 123 (1), 443–463. http://dx.doi.org/10.1002/2017JA024499.

Roussos, E., Krupp, N., Paranicas, C., Kollmann, P., Mitchell, D.G., Krimigis, S.M., Palmaerts, B., Dialynas, K., Jackman, C.M., 2018. Heliospheric conditions at Saturn during Cassini's ring-grazing and proximal orbits. Geophys. Res. Lett. 45 (20), 10812–10818. http://dx.doi.org/10.1029/2018GL078093.

Taubenschuss, U., Cecconi, B., Lamy, L., 2021. Catalogue of Faraday Rotation Patches Identified in Saturn Kilometric Radiation (SKR) Observations By Cassini/RPWS/HFR (Version 1.0) [Data Set]. PADC, http://dx.doi.org/10.25935/R11G-6J63.

Taubenschuss, U., Santolík, O., 2019. Wave polarization analyzed by singular value decomposition of the spectral matrix in the presence of noise. Surv. Geophys. 40, 39–69. http://dx.doi.org/10.1007/s10712-018-9496-9.

Thompson, A.R., Moran, J.M., Swenson Jr., G.W., 2017. Interferometry and Synthesis in Radio Astronomy, third ed. In: Astronomy and Astrophysics Library, Springer, http://dx.doi.org/10.1007/978-3-319-44431-4.

Thomsen, M.F., Coates, A.J., 2019. Saturn's plasmapause: Signature of magnetospheric dynamics. J. Geophys. Res. 124, 8804–8813. http://dx.doi.org/10.1029/2019JA027075.

Thomsen, M.F., Jackman, C.M., Mitchell, D.G., Hospodarsky, G., Kurth, W.S., Hansen, K.C., 2015b. Sustained lobe reconnection in Saturn's magnetotail. J. Geophys. Res. 120, 10257–10274. http://dx.doi.org/10.1002/2015JA021768.

Thomsen, M.F., Mitchell, D.G., Jia, X., Jackman, C.M., Hospodarsky, G., Coates, A.J., 2015a. Plasmapause formation at Saturn. J. Geophys. Res. 120, 2571–2583. http://dx.doi.org/10.1002/2015JA021008.

Vasyliunas, V.M., 1983. Plasma Distribution and Flow, in Physics of the Jovian Magnetosphere. Cambridge Univ. Press, New York, pp. 395–453,

Vogl, D.F., Cecconi, B., Macher, W., Zarka, P., Ladreiter, H.-P., Fédou, P., Lecacheux, A., Averkamp, T., Fischer, G., Rucker, H.O., Gurnett, D.A., Kurth, W.S., Hospodarsky, G.B., 2004. In-flight calibration of the Cassini-radio and plasma wave science (RPWS) antenna system for direction-finding and polarization measurements. J. Geophys. Res. 109, A09S17. http://dx.doi.org/10.1029/2003JA010261.

Warwick, J.W., Dulk, G.A., 1964. Faraday rotation on decametric radio emissions from Jupiter. Science 145, 380–383. http://dx.doi.org/10.1126/science.145.3630.380.

Warwick, J.W., Pearce, J.B., Evans, D.R., Carr, T.D., Schauble, J.J., Alexander, J.K., Kaiser, M.L., Desch, M.D., Pedersen, M., Lecacheux, A., Daigne, G., Boischot, A., Barrow, C.H., 1981. Planetary radio astronomy observations from Voyager 1 near Saturn. Science 212, 239–243. http://dx.doi.org/10.1126/science.212.4491.239.

Went, D.R., Hospodarsky, G.B., Masters, A., Hansen, K.C., Dougherty, M.K., 2011. A new semiempirical model of Saturn's bow shock based on propagated solar wind parameters. J. Geophys. Res. 116, A07202. http://dx.doi.org/10.1029/2010JA016349.

Wu, C.S., Lee, L.C., 1979. A theory of the terrestrial kilometric radiation. Astrophys. J. 230, 621–626. http://dx.doi.org/10.1086/157120.

Ye, S.-Y., Fischer, G., Kurth, W.S., Menietti, J.D., Gurnett, D.A., 2018. An SLS5 longitude system based on the rotational modulation of Saturn radio emissions. Geophys. Res. Lett. 45, 7297–7305. http://dx.doi.org/10.1029/2018GL077976.

Ye, S.-Y., Gurnett, D.A., Fischer, G., Cecconi, B., Menietti, J.D., Kurth, W.S., Wang, Z., Hospodarsky, G.B., Zarka, P., Lecacheux, A., 2009. Source locations of narrowband radio emissions detected at Saturn. J. Geophys. Res. 114 (A06219), http://dx.doi.org/10.1029/2008JA013855.

Zarka, P., 1998. Auroral radio emissions at the outer planets: Observations and theories. J. Geophys. Res. 103, 20159–20194. http://dx.doi.org/10.1029/98JE01323.